LITHOS 484-485 (2024) 107748

Contents lists available at ScienceDirect

LITHOS

journal homepage: www.elsevier.com/locate/lithos

Kyanite microstructural and microchemical characteristics reveal differences in growth, deformation and chemical modification: A case study from the Paleoproterozoic suture zone of South Harris, NW Scotland

Eleanore Blereau [a,b,*], Sandra Piazolo [a], Patrick Trimby [c,d], Etienne Skrzypek [e]

[a] Institute of Geophysics and Tectonics, School of Earth and Environment, The University of Leeds, UK
[b] Department of Geology and Geological Engineering, Faculty of Science and Engineering, Université Laval, Québec, Canada
[c] Oxford Instruments Nanoanalysis, High Wycombe, UK
[d] Carl Zeiss Ltd., Cambourne, Cambridge, UK
[e] University of Graz, Institute of Earth Science – NAWI Graz Geocenter, Graz, Austria

ARTICLE INFO

Keywords:
Kyanite
EBSD
Partial melting
Trace elements
Deformation mechanisms
Outer Hebrides

ABSTRACT

Based on petrological association, cathodoluminescence (CL), trace element signatures and orientation relationships, two generations of kyanite are distinguished in a high temperature, high pressure garnet-biotite-aluminosilicate bearing migmatite of South Harris, NW Scotland. The migmatite shows a garnet and biotite rich domain (*Grt-Bt domain)* which is cut at a low angle by a dominantly coarse-grained plagioclase-quartz leucosome. In addition, a fine-grained plagioclase-quartz-kyanite domain (*Plag-Qtz-Ky domain*) is present intercalated with the *Grt-Bt domain* and subparallel to the plagioclase-quartz domain. Type 1 kyanite is coarse grained and associated with Bt clusters and garnet within the *Grt-Bt domain*. It grew relatively early, *syn-* to post-garnet growth, in a suprasolidus environment resulting in crystallographically determined oscillatory CL and trace element zoning. Grains record evidence of progressive deformation in the crystal plastic regime, where deformation is accommodated by dislocation glide, climb and deformation twinning. The dominant activated slip system is (100)<001> with minor component of <100>, while deformation twins show a ~ 180° rotation around ~<001> axis and a twin plane near (001). Grains appear to be impervious to deformation induced diffusion with all zoning remaining sharp despite crystal plastic deformation. Grains in direct contact with the *Plag-Qtz-Ky domain* show late modification of the CL and trace element signature suggesting melt-mediated interface-coupled dissolution-precipitation reaction. This modification resulted in crosscutting lobate high trace element regions and irregular rims with low Cr and V content. These rims show similar CL and trace element characteristics as Type 2 kyanite which are exclusively seen within the *Plag-Qtz-Ky domain* suggesting that Type 2 grains are cogenetic with Type 1 rims. Type 2 grains are finer grained than Type 1 grains and show near uniform CL and trace element distributions with rare oscillatory zoned and relatively higher Cr & V bright cores. Type 2 show either no or very localized internal deformation features. However, they exhibit a clear shape preferred orientation which coincides with a crystallographic preferred orientation where the longest shape axis is parallel to <001>. We propose that Type 2 kyanite grains underwent melt-present deformation by rigid body rotation in an externally derived melt with different trace element chemistry than the host rock. This melt thus interacted chemically by melt-mediated interface-coupled dissolution-precipitation reactions with the surrounding rocks forming the Type 1 rims.

Our study shows detailed analysis of kyanite is an important tool for giving constraints on the deformation, *P–T* and melting history of high-grade metamorphic rocks and migmatites.

1. Introduction

Kyanite is a mineral common within medium to high pressure metamorphic rocks and at sub- to suprasolidus conditions. Kyanite is primarily used for metamorphic pressure constraints but is rarely utilized further by petrologists, except for its relationship to deformational

* Corresponding author at: Institute of Geophysics and Tectonics, School of Earth and Environment, The University of Leeds, UK.
E-mail address: eleanore.blereau.1@ulaval.ca (E. Blereau).

https://doi.org/10.1016/j.lithos.2024.107748
Received 14 March 2024; Received in revised form 26 July 2024; Accepted 6 August 2024
Available online 13 August 2024

fabrics. Kyanite, although a common mineral, can result from several different mineral reactions, such as partial melting reactions. Kyanite can be xenocrystic and/or crystallize from melt directly (Phillips et al., 2023), making it difficult to pinpoint its origin and paragenetic history through time. Kyanite very often occurs in deformed rocks, with grains often containing internal deformational features such as kink bands and undulose extinction (Boland et al., 1977; Lefebvre and Menard, 1981). Kyanite can exhibit lamella growth twins on (100) and also has a number of cleavages (perfect on {100}, good on {010} (Deer et al., 2013). Kyanite can incorporate an array of trace elements (Albee and Chodos, 1969; Chinner et al., 1969; Deer et al., 2013; Herz and Dutra, 1964; Neiva, 1984; Pearson and Shaw, 1960; Phillips et al., 2023; Yang and Rivers, 2001), including Cr and V at the ppm level. Recently, it has been shown that internal sector and oscillatory cathodoluminescence (CL) zoning and intensity correlates well with trace element concentrations (Kendrick and Indares, 2018; Müller et al., 2003; Peterman et al., 2021; Phillips et al., 2023) and that zoning and trace elements can be used to differentiate between sub-solidus kyanite growth, xenocrystic grains and growth related to partial melting (Kendrick and Indares, 2018; Phillips et al., 2023).

While the different nature of zonation patterns of kyanite opens up new possibilities to investigate a range of geological processes, the behaviour and partitioning of trace elements incorporated in or lost from kyanite through different processes such as growth, reactions and deformation remains currently unknown. For example, it has been shown in recent years that defect structures associated with internal deformation features can have major effects on the major, trace element and isotope chemistry of minerals and can reset or modify their recorded information. This mostly occurs through the movement of dislocations mobilizing trace elements, as well as by dislocation arrays that provide fast diffusion pathways (e.g. zircon (Piazolo et al., 2016, Piazolo et al., 2012); pyroxene (e.g. Lund et al., 2006); titanite (e.g. Corvò et al., 2023)). In addition, fluid-mediated interface coupled replacement reactions (e.g. Putnis, 2009) may significantly change the elemental composition of minerals (Corvò et al., 2023; Varga et al., 2020).

Crystal plastic deformation is induced by differential stress and is facilitated by the generation, movement and self-organization of dislocations resulting in permanent strain. This movement of dislocations causes a change of orientation within a single grain otherwise known as lattice distortion which is observed as undulose extinction. If dislocations are rearranged during recovery this can be recognised by the presence of low angle boundaries. The latter features are key indicators of crystal plasticity along with grain size reduction by dynamic recrystallization, the development of crystallographic preferred orientations (CPO) and shape preferred orientation (SPO) of a population of grains (e.g. see review by Daczko and Piazolo, 2022 and references therein). Crystal plasticity is dominant at high stresses and large grain sizes and elevated temperatures in rocks in the solid state (Frost and Ashby, 1982). Even if low percentages of melt (e.g. 7–8%) are present within the grain boundary network, e.g. during incipient partial melting, deformation may mainly occur by crystal plasticity (Rosenberg and Handy, 2005 and references therein; Gleason et al., 1999; Hirth and Kohlstedt, 1995a, 1995b; Mei et al., 2002; Walte et al., 2005). Deformation remains governed by the solid phases. However, at higher melt percentages, the solid phase framework is lost and the rheology is governed by the viscosity of the melt itself resulting in a significant strength decrease and rheological change (Beaumont et al., 2001; Rosenberg and Handy, 2005). Such melt-present deformation is recognised by limited or complete lack of internal plastic deformation within the minerals within the deforming melt, with these minerals also displaying a shape preferred orientation (SPO) with or without a CPO coupled with melt-related microstructures (Daczko and Piazolo, 2022; Ghatak et al., 2022; Stuart et al., 2018; Vernon, 2011). Here, the solid phases deform predominately by rigid body rotation unless several of the solid phases cluster and form a local solid framework (e.g. Shao et al., 2021). Therefore, through the application of careful microstructural analysis and quantitative orientation analysis such as Electron Backscatter Diffraction (EBSD), it is possible to identify and differentiate the deformation processes active within in a rock during its solid state, partially melted and melt-dominated evolution.

In the following, we investigate if kyanite can be used not only as a *P–T* indicator but also as a tool to unravel the evolution of a high-grade metamorphic rock that has undergone several phases of deformation and evolution in the presence of melt. We investigate the kyanite grains and their textures through optical microscopy, backscatter electron (BSE) imaging, petrology, CL imaging, quantitative orientation analysis using EBSD coupled with energy dispersive X-ray spectrometry (EDS), and electron microprobe (EPMA) trace element mapping. Our study shows that detailed analysis of kyanite provides unprecedented insight into the growth, deformation and modification processes at high-grade conditions.

2. Regional geology

Our case study takes advantage of a kyanite rich, high strain, high grade metapelitic sample stemming from the metasedimentary Chaipaval Series in the north of the Leverburgh Belt of South Harris, NW Scotland (Fig. 1). The sample has been selected based on its abundance of kyanite grains of different characteristics and its known complicated *P–T* path (Baba, 2004; Hollis et al., 2006) for which the deformation history remains largely unknown (for details see below). The metamorphic evolution of South Harris in the Outer Hebrides is of general interest as the region is made up of a number of Archean basement terranes with distinct geological histories that were later amalgamated (Friend and Kinny, 2001; Kinny et al., 2005). South Harris, also sometimes called the Roineabhal Terrane, represents a suture zone between the Uist Block to the south and Tarbet Terrane to the north as a remnant Paleoproterozoic continental volcanic arc (Baba et al., 2012). This this region is a valuable place to study as our understanding of terrane amalgamation during the Palaeoproterozoic is still largely lacking.

The Leverburgh Belt is interpreted to represent an accretionary prism that was subducted, intruded by magmas in an arc or marginal setting followed by accretion of rifted microcontinents, exhumation and then deformation (Baba et al., 2012). The Leverburg Belt is composed of three series: Benn Obbe, Rodel and Chaipaval Pelitic Series (Baba et al., 2012; Dearnley, 1963). The timing of these events however remains poorly constrained. A previous study identified ultra-high temperature (UHT) metamorphism in rocks near the South Harris Igneous Complex in the south of the Leverburgh Belt (Baba, 1999; Baba, 2003). This metamorphism followed an anticlockwise *P–T* path with M1 at 900–980 °C and 9–11 kbar in sillimanite stability followed by a later higher-pressure event (M2) around 850–900 °C and 13–14 kbar in kyanite stability (Baba, 2004; Hollis et al., 2006). This was followed by decompression (M3) and hydrous retrogression (M4) (Baba, 1998; Baba et al., 2012).

The sample SH2009 was collected from the northern extension of the Leverburgh Belt within the Chaipaval Pelitic Series (57° 48′ 29.59" N, 7° 5′ 18.27" W; Fig. 1B). In the outcrop the foliation strikes roughly N (352° to 005°) and dips steeply (62° to 72°) to the east. The sample is taken close to the boundary to the Ben Obbe series otherwise called the Ben Obbe Quartzites (Dearnley, 1963) which has been interpreted to be characterized by trench-type sediments and arc-type volcanics (Baba et al., 2012).

3. Methods

3.1. Sample preparation

The sample was prepared for a thin section by cutting parallel to the lineation (x direction) and perpendicular to the foliation (z direction). The 30 μm thick thin section was mechanically polished down to 0.5 μm. A final chemo-mechanical polish was conducted using a 0.04 μm colloidal silica solution to allow for quantitative orientation analyses.

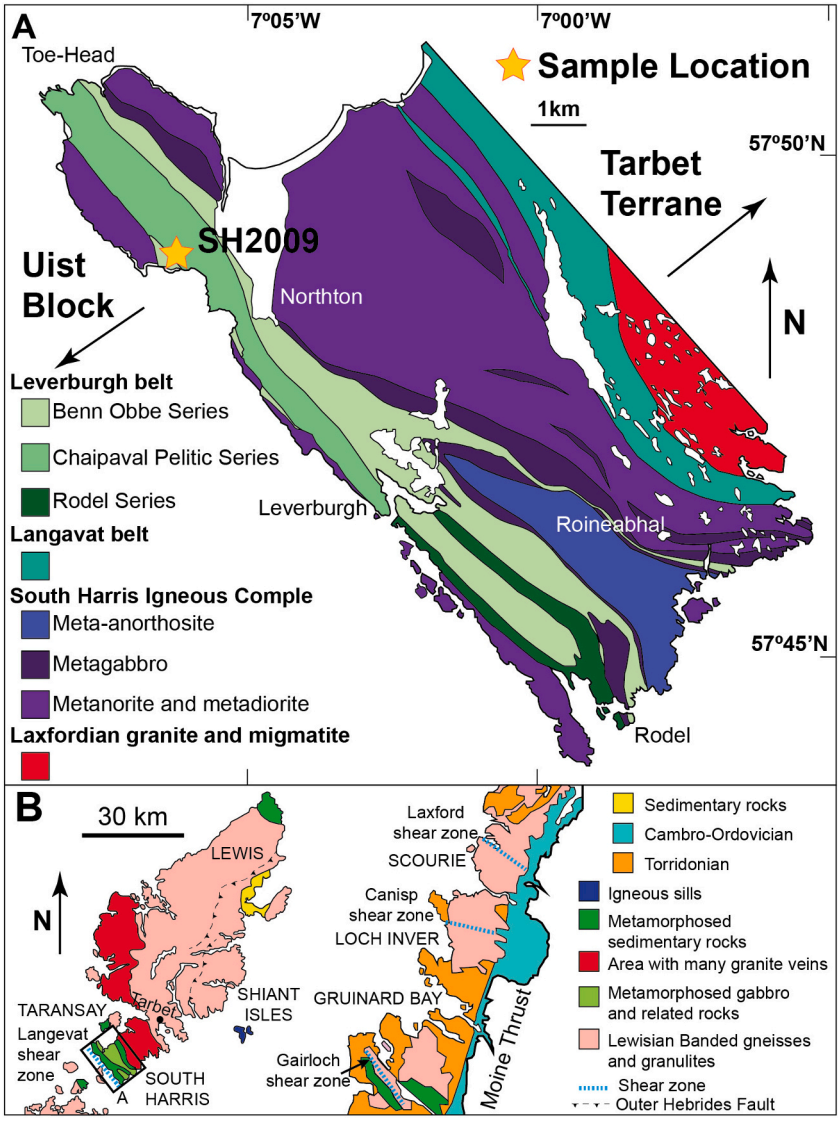

Fig. 1. A) Geological map of South Harris, modified after Baba et al. (2012). B) Overview geological map of Lewis, Harris and Scotland modified after Goodenough et al. (2011).

The sample was then coated with a thin carbon coat (~5–10 nm). After CL analysis, the thin section was repolished with colloidal silica and re-carbon coated.

3.2. SEM based analyses

SEM analysis such as CL and BSE imaging, and EDS and EBSD analysis was conducted within the LEMAS centre at the University of Leeds. Panchro CL and BSE Imaging was conducted on a TESCAN VEGA3 XM under the conditions of Peterman et al. (2021); ~15 mm working distance, with 18 kV and 1–3 nA beam. Quantitative orientation and chemical mapping (EBSD and EDS) was conducted initially at the Oxford Instrument Nanoanalysis Application Laboratory (High Wycombe, UK). The data were collected using a Hitachi SU-70 Field Emission SEM equipped with an Oxford Instruments AZtec Integrated EDS and EBSD system with a Symmetry S2 EBSD Detector and UltimMax 65 EDS detector. A large-scale map made up of 480 individual maps was collected over 44 h with a raster of 4 μm measurement step size. Beam energy was 20 keV and beam current was 24.9 nA.

Additional smaller scale maps with higher spatial resolution were acquired at the LEMAS centre at the University of Leeds using the Oxford Instruments Symmetry S2 EBSD Detector and EDS detector on a field emission gun FEI Quanta 650. Step sizes varied from 0.2 μm to 1 μm depending on grain size. All maps were processed using AZtecCrystal by Oxford Instruments. The degree of plastic deformation is assessed using profiles of orientation changes and in Grain Reference Orientation Deviation (GROD) angle maps which take the average orientation of each grain and shows the relative disorientation for each pixel, with disorientation being defined as the smallest possible misorientation. The Weighted Burgers Vector (WBV) analysis function within AZtecCrystal (Wheeler et al., 2009, 2024) was used to identify the dominant slip system in regions of deformation. WBV's were calculated using a sliding integral loop method, based on a square 7 × 7 pixel array about each measurement point. WBV magnitudes below a threshold value have been disregarded (minimum magnitude of 10%). Upper hemisphere pole figures are used to assess crystallographic preferred orientation and the extent and nature of lattice dispersions of individual grains or grain clusters. Pole figures plot data in two ways: (i) showing all data within selected grains (cf. Fig. 6A,D; Fig. 7B,G; Fig. 9D) to highlight the orientation changes within individual, representative grains (points are shown in the same colour scheme as in the map), and (ii) one-point-per-crystallite if the bulk crystallographic preferred orientation is to be assessed (cf. Fig. 6A, 7B, 9A). Which method is used is noted in the figure captions. A crystallite is defined as an area enclosed by grain boundaries

of >10° misorientation.

3.3. Major and trace element mapping

Qualitative trace element EPMA maps were undertaken to better differentiate between different CL zones and correlate or differentiate between different generations of kyanite. Electron microprobe X-ray maps were conducted on a JEOL 8230 EPMA in the LEMAS centre, University of Leeds with five WDS spectrometers. Operating conditions were set at 20 kv and 400 nA fully focused with a 10 s dwell time. P was measured on 3 separate spectrometers (PETJ, PETJ and PETH) with all counts from all three spectrometers summed together. V was measured on LIFL and Cr on LIFH. Additionally, as we had high intensity visible CL zoning the Fe concentration of our kyanite was unlikely to be of much interest as Fe is a CL quencher (Peterman et al., 2021; Phillips et al., 2023). Pixel size utilized for mapping varied between 2 and 4 μm. The software used to collect the maps was 'Probe for EPMA' module 'Probe Image' produced by 'Probe Software' (https://www.probesoftware.com/PI_Features.html).

A further microprobe map was performed at the University of Graz using a JEOL JXA-8530F Plus electron microprobe equipped with five wavelength-dispersive spectrometers. Operating conditions were 15 kV accelerating voltage and 200 nA beam current in focused beam mode. The Kα lines of Ti (PETJ), P (TAP), V (PETL), Cr (PETH) and Fe (LIF)

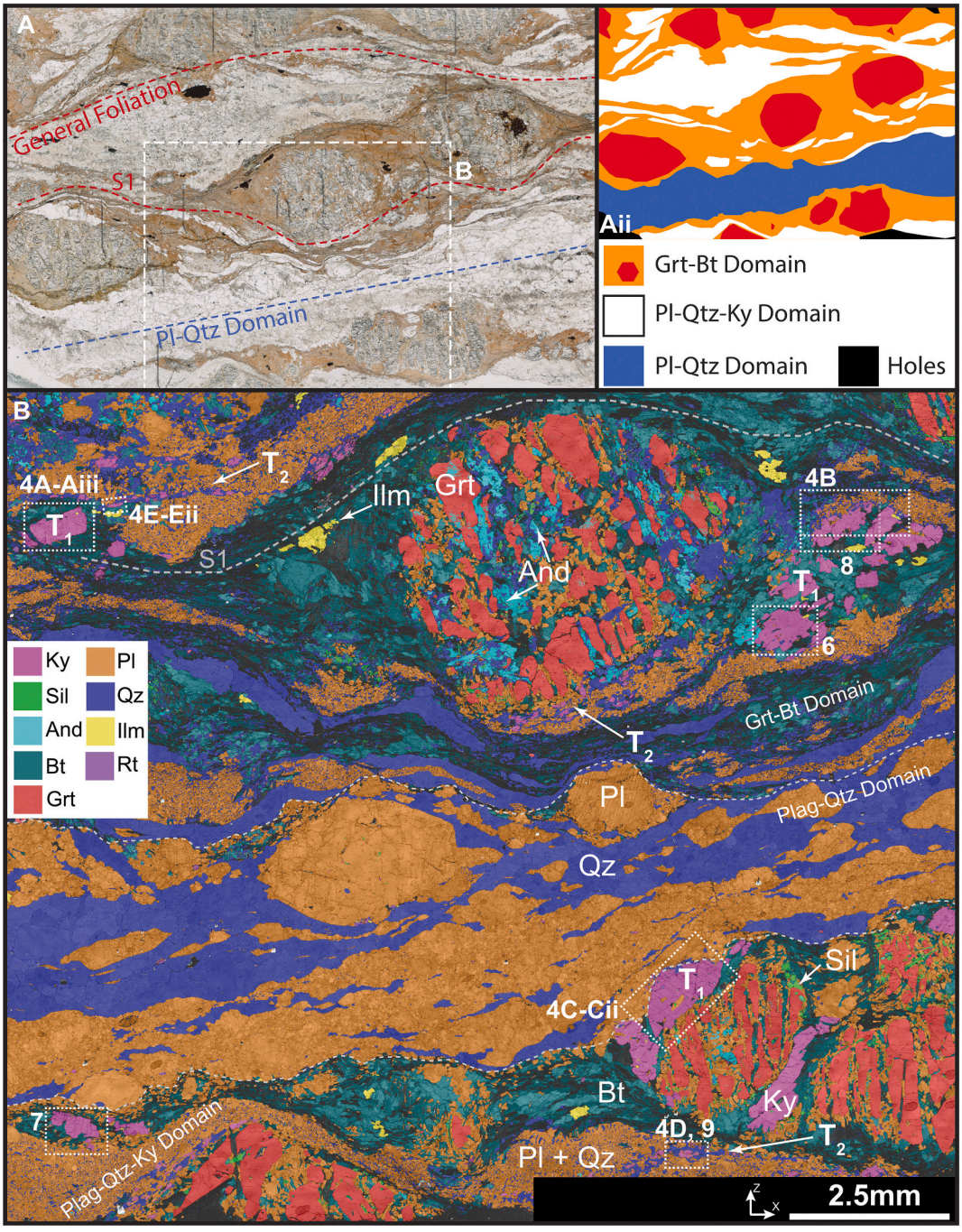

Fig. 2. A) Plane polarised light image of SH2009 thin section. Aii) Simplified diagram of different domains identified within A. B) EBSD derived phase + band contrast map of part of SH2009, showing porphyroblastic garnet with biotite strain shadows and caps, injected leucosome with large plagioclase crystals, local melt represented by plagioclase + quartz and Type 1 (T_1) and 2 (T_2) kyanite. White fine dashed boxes indicate location of other analyses in later numbered figures.

were measured for 20–30 ms dwell time in stage scan mode (0.5–1 μm step size). All maps were background corrected and high trace element inclusions were removed using XmapTools3 (Lanari et al., 2014).

4. Results

4.1. General sample description

The sample studied is characterized by a distinct foliation defined by the alignment of biotite and kyanite which wraps around up to 0.5 cm large garnets. It is representative for the migmatitic part of the series characterized by up to 1 cm thick plagioclase-quartz dominated leucosomes with minor biotite which can be continuous over several meters. In thin section, three domains are clearly visible (Fig. 2A, Aii). The host to the plagioclase-quartz dominated leucosomes (*Plag-Qtz domain*), is a strongly foliated aluminosilicate-bearing garnet-biotite gneiss defining a second *Grt-Bt domain*. Intermingled with and between layers of the host *Grt-Bt domain* is a distinctly finer grained third *Plag-Qtz-Ky domain* also

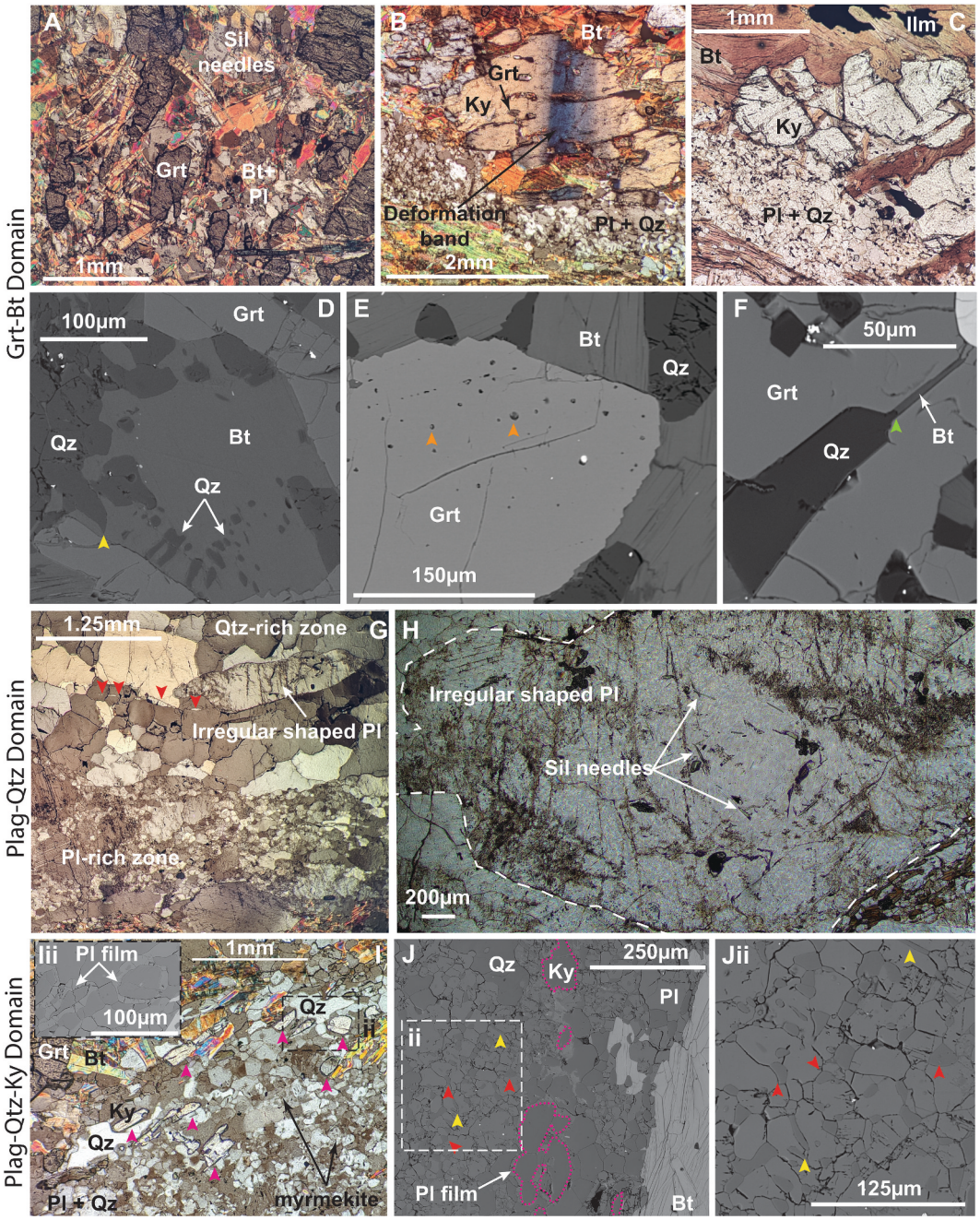

Fig. 3. A) Fragmented garnet with needles of sillimanite. B) Type 1 kyanite showing strong undulose extinction. C) Type 1 kyanite next to melt pseudomorph. D) BSE image showing low dihedral angle grain of quartz (yellow arrow) with biotite which also contains small blebs of quartz. E) BSE image showing polycrystalline inclusions in garnet (orange arrows). F) BSE image showing elongate biotite grain sharing an concave grain boundary with quartz (green arrow) in garnet. G) Photomicrograph of the *Plag-Qtz domain* showing large and often tapered xenocrystic plagioclase and elongate chains of plagioclase grains in quartz-rich areas (red arrows). H) Inclusions of sillimanite needles within a xenocrystic plagioclase grain. I) Small Type 2 kyanite with films of plagioclase marked by pink arrows. Iii) BSE image of plagioclase films around kyanite. J) BSE image of Type 2 kyanite in melt pseudomorph, kyanite delineated by pink lines. Jii) Inset showing elongate quartz grains (yellow arrows) in intergrown plagioclase + quartz melt pseudomorph as well as curved quartz grains pools at triple junctions (red arrows). (For interpretation of the references to colour in this figure legend, the reader is referred to the web version of this article.)

rich in plagioclase and quartz but containing fine grained aluminosilicate grains.

The host *Grt-Bt domain* is dominated by biotite, aluminosilicate and garnet with minor quartz and ilmenite, zircon and monazite as accessory phases. The garnet porphyroblasts (0.2–0.5 cm) are inclusion free in the core. Towards the edge of garnet grains, some sillimanite grains are seen as inclusions (Fig. 3A) which exhibit a shape preferred orientation. Garnets are seen as fragments, however, original grains are clearly distinguishable, as they retain their largely equidimensional shape suggesting little displacement associated with fragmentation (Fig. 2A). Biotite is mm sized and occurs dominantly in the *Grt-Bt domains*. It defines the primary foliation (S_1), wraps around garnet (Figs. 2B, 3A–C) and occurs in garnet strain shadows (Fig. 2B). Elongate quartz grains form low dihedral angles with biotite and rounded blebs within biotite (Fig. 3D). Quartz also occurs within polymineralic inclusions (Quartz and plagioclase) within garnet (Fig. 3E) and forms interstitial microstructures next to biotite and plagioclase (Fig. 3F).

The *Plag-Qtz domain* is predominantly made up of plagioclase and quartz with accessory phases including zircon, minor small monazite and rutile that is often associated with ilmenite and zircon. Plagioclase occurs as large, ~1–3 mm, irregular grains that often have rounded to elongate grain shapes with tapered ends, multiple twinning and inclusions of rare sillimanite needles (Figs. 2B, 3G, H). These large plagioclase grains are commonly surrounded by quartz that vary in grain size from ~0.2 mm to over 1 mm and wrap around the plagioclase. Plagioclase 'string of beads' and grains with very low dihedral angles also occur within the quartz rich regions (Fig. 3G). Regions dominated by predominantly finer plagioclase also occur with smaller quartz lenses. This domain appears to crosscut the samples primary foliation defined by the *Grt-Bt domain* at a low angle and does not contain any apparent reaction textures.

The *Plag-Qtz-Ky domain* is made of plagioclase, quartz, kyanite with rare muscovite, biotite, ilmenite and zircon. This domain is consistently fine grained regardless of the phase (~500 μm or less) where plagioclase and quartz is intergrown with common sections of myrmekite (Figs. 2B, 3I–Jii). In addition to myrmekite, highly elongated quartz occurs between plagioclase grains and quartz grains with curved boundaries often occur at triple junctions (Fig. 3J–Jii).

All three aluminosilicates are present within the sample, identified through EBSD, with their own discrete populations and little to no evidence of obvious sequential replacement that can be seen within some other triple aluminosilicate samples (Whitney and Samuelson, 2019). Only in a few instances, very rare sillimanite inclusions are seen in Type 1 kyanite with an epitaxial relationship. Andalusite is present primarily within the fractures in garnet (Fig. 2B) while sillimanite is seen included in the rims of garnet and within the biotite-rich matrix (Figs. 2B, 3A). Kyanite occurs within biotite rich areas (Fig. 3B–C) and *Plag-Qtz-Ky domain* and will be discussed in detail below.

4.2. General microstructural and microchemical characteristics of kyanite populations

Kyanite occurs as two distinct populations defined by their microstructural and paragenetic association and grain size.

Type 1 – Kyanite in host Grt-Bt domain: Kyanite grains are ~400 μm to ~1 mm in length and are either in biotite rich areas or in the biotite-rich strain shadows/caps of garnet porphyroblasts (Fig. 2B); in some case they are in close proximity to the *Plag-Qtz-Ky domain* (Fig. 2).Type 1 kyanite does not occur as inclusions within garnet but rare garnet inclusions do occur within Type 1 kyanite (Fig. 3B). Grains are blocky, subhedral to anhedral (Figs. 2B, 3B, C) with sometimes irregular grain boundaries (Fig. 3B, C). All grains exhibit significant undulose extinction commonly forming near parallel bands crossing the grain (Fig. 3B). Some coarse grains display well defined, internal structures typical for twinning. Type 1 kyanite may contain inclusions of biotite, rutile, ilmenite, quartz, plagioclase and very rarely sillimanite and garnet.

Type 2– Kyanite in the Plag-Qtz-Ky domain: Type 2 kyanite grains vary from equant to roughly elliptical in shape (Fig. 3I) and often occur in clusters. They occur in the *Plag-Qtz-Ky domain* that can be located nearby garnet in the host *Grt-Bt domain* (Figs. 2B, 3I). Grains are rimmed by plagioclase and then are in turn surrounded by quartz (Fig. 3I–J). Type 2 kyanite grains are distinctly smaller, on average 100 μm in size (Fig. 3I–J). Only a small number of grains shows slight undulose extinction, these are exclusively within kyanite clusters. Type 2 kyanite does not contain inclusions.

4.3. Cathodoluminescence signatures

Type 1 kyanite grains have predominantly quite simple internal CL textures, with internal zones of moderate grey, homogeneous CL response, hereafter referred to as cores (Fig. 4A–C). Within the cores, faint fine-scale oscillatory zoning can be found that aligns with the crystal facets (Fig. 4A, Aii).

The zoning within these cores is sometimes crosscut by partial rims or lobate zones that have variable CL response (Fig. 4B, C). Bright CL zones most often transition into dark CL response regions towards the outer edge of the grain (Fig. 4B–C) and dark CL zones rarely occur in the more inner parts of the grain (Fig. 4B). Bright and dark CL response zones often occur together in pairs (Fig. 4B, C). These zones have sharp edges and can also be seen to truncate other pairs of bright and dark CL zones (Fig. 4B). Regardless of whether the grains show undulose extinction or twinning the CL zoning remains sharp and uninterrupted. The grains that show the lobate zones also have an irregular shaped dark CL response rim at their outermost edge (Fig. 4B–C). The grains with these lobate zones and rims occur only when Type 1 kyanite is in direct contact with the *Plag-Qtz-Ky domain* (Fig. 4B–Cii).

Type 2 grains are distinct in CL response, showing almost uniform dark CL response with only subtle oscillatory zoning and sometimes show small brighter cores (Fig. 4D–Eii). The relative intensity of their CL response is similar to the outermost darker CL response rims sometimes seen on Type 1 grains (c.f. Fig. 4B, C).

4.4. Trace element patterns based on EPMA mapping

EPMA maps were taken from representative Type 1 and Type 2 grains (for spatial context the reader is referred to Fig. 4A–D). The elements of Cr and V exhibited the most pronounced variation while element P was mostly homogeneously distributed. Ti showed no significant zoning so the data are not presented.

Cr and V concentration patterns correlate very well with CL zoning and relative CL response of the mapped grains. For example, the moderate grey CL response Type 1 cores show moderate concentrations of trace elements as well as the preservation of the often-subtle zoning features dependent on analysis resolution, including the observed oscillatory zoning (Fig. 5A–K). P often shows minimal variation, it is a very low signal, but occasionally highlights zoning within the medium grey areas (Fig. 5B). The lobate bright CL response cross cutting zones show consistently higher trace element levels than the moderate grey cores particularly for Cr and V (Fig. 5A, C, D, F, G, I). These zones most often exhibit normal zoning (from high to low towards the outside of the grain) but can also display reverse zoning (low to high towards the outside of the grain) within a single zone (Fig. 5C, F, I). These enriched zones are often followed by the least concentrated regions that correlate with the darkest CL response (Fig. 5C, F). The outermost portion of grains showing these lobate features display the lowest trace element concentrations recorded within irregularly shaped rims (Fig. 5D, F, G, I).

In contrast to Type 1 kyanite, Type 2 kyanites show consistently low levels of trace elements, with any variations correlating with the subtle internal CL zoning that is also consistently low in response (Fig. 5L–N).

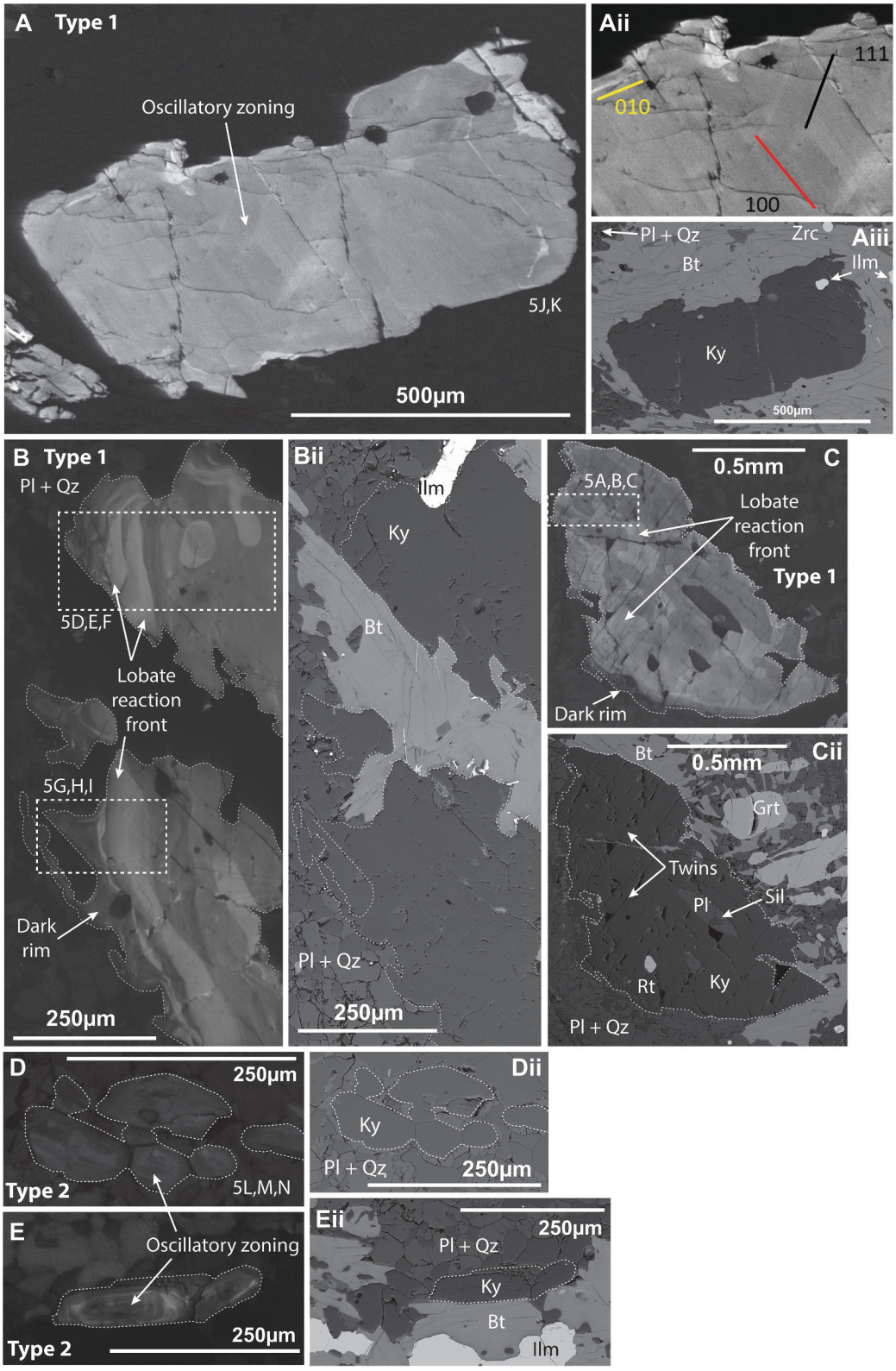

Fig. 4. A) Type 1 kyanite with large moderate grey CL response core illustrating faint oscillatory zoning. Aii) Annotated crystallographic facets that align with oscillatory zoning. Aiii) BSE image relating to A and Aii. B) Multiple overprinting pairs of reaction fronts with each bright CL response zone followed by dark CL response outer rim/irregular growth. Dashed grey line highlights edge of grains. Dashed white boxes corresponds to EPMA maps in Fig. 5D–I. C) Type 1 kyanite with lobate cross-cutting bright CL response zones followed by dark CL response outermost rim. Dashed grey line highlights edge of grains. Dashed white box corresponds to EPMA maps Fig. 5A–C. Cii) BSE image relating to C, linear twins are visible. D–E) Type 2 kyanite showing overall dark CL response and oscillatory zoning. D is the grains within EPMA map Fig. 5L–N. Dii–Eii) BSE image relating to D and E respectively.

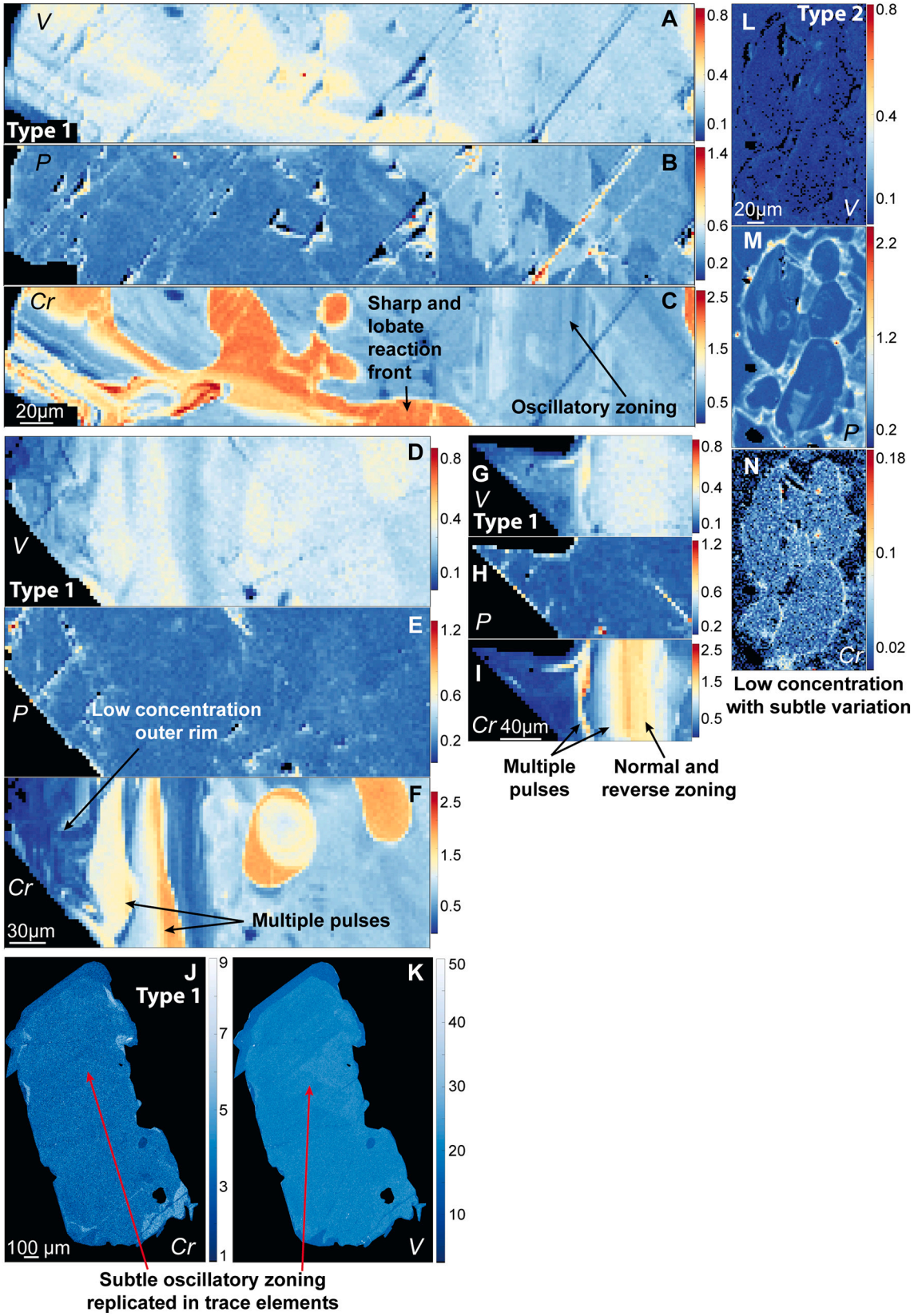

Fig. 5. EPMA trace element maps. A–C) Type 1 bent and twinned kyanite shows moderate trace element concentrated core with relatively enriched lobate cross cutting zones in V and Cr. Some variation in P correlating with zoning in Cr. D—F) Type 1 bent kyanite with two lobate zones that crosscut each other as well as low concentration outermost rim. G–I) Type 1 bent kyanite with normal and reverse zoned enriched zone in Cr and V with low concentration outer rim. J–K) Type 1 kyanite with subtle oscillatory zoning, finest zones seen in CL correlate with Cr and more broader zones with V (conducted at Graz). L–N) Type 2 kyanite that is generally low in concentration (different scale) with correlation between Cr, V and P. M and N are not scaled the same as the other maps in order to best highlight subtle features.

4.5. Quantitative crystal orientation and shape preferred orientation characteristics

Type 1 grains show a weak crystallographic preferred orientation (CPO) (Fig. 6A) with a general alignment of the c-axis lying within the foliation of the sample, while a and b axes are close to random. This kyanite type has a shape preferred orientation (SPO) subparallel to the main foliation (Fig. 6B).

Type 1 kyanite grains show variable internal lattice distortion, however no kink bands sensu stricto are observed. Areas of continuous lattice bending are up to ~100 μm wide (Figs. 3D, 6C) and show mostly low angle misorientation of up to ~20° per 100 μm (Fig. 6C; orange-red regions) reaching in some grains more rarely up to >30° of change in orientation. Little lattice distortion is seen parallel to these distortion bands (<1°; Fig. 6Ciii). Pole figures indicate systematic deformation with a consistent rotation axis around <010> (Fig. 6D).

The Weighted Burgers Vector (WBV) map shows the dominant WBV is close to the <001>(Fig. 6E). Low angle misorientation axes mirror the dominant rotation axis of <010> seen in Fig. 6D with a minor input near approximately <114> (Fig. 6F). The dominant slip system was determined to be along the (100) plane and in the <001> direction (red in Fig. 6G) with a minor contribution from <100> seen as scattering along the slip plane in Fig. 4E (blue-green in Fig. 6E). Some of the Type 1 grains also show the presence of straight, low angle (<10°) subgrain boundaries that dominantly develop parallel with the edges of a deformation band (Fig. 7A).

Some Type 1 grains show evidence of twinning (Fig. 7). The twinned Type 1 grains show lattice bending (Fig. 7A) with the same <010> rotation axis (Fig. 7B, E) and dominant (100)<001 > slip system (Fig. 7C, F) as well as the minor <100> contribution, albeit with less dispersion (Fig. 7F) (Fig. 7E). The twin boundaries are distinct and systematic, with ~180° of rotation around <−10–4>, and a (001) twin plane (Fig. 7G-Gii). The twins show slight tapering along their length and may occur slightly oblique to the deformation bands (Fig. 7A, A*). In addition, these grains show a range of internal deformation features including subgrain boundaries with misorientations of 2–6° with adjacent portions still showing some continuous lattice bending (Fig. 7Ai) and subgrains with little internal lattice bending i.e. orientation plateaus adjacent to subgrain boundaries reaching close to 10° misorientation (Fig. 7Aii).

The regions of Type 1 kyanite grains in direct contact to the *Plag-Qtz-Ky domain* which are characterized by bands of moderately high CL response that crosscut the oscillatory banding. These high Cl zones transition into an irregular dark CL outermost rim exhibit different lattice deformation features compared to the moderate CL response cores.

Firstly, these lobate and dark rim regions rarely exhibit subgrain boundaries despite being at the edge of crystals. This contrasts with the comparatively straight subgrain boundaries found in the original cores (Fig. 8). Secondly, these regions show relatively more dispersion when the low angle misorientation axes are plotted compared to the core regions (Fig. 6 pole figures).

The population of Type 2 grains show a moderate CPO coupled with a strong SPO (Fig. 9A–B). Type 2 kyanites have distinctively different features of internal lattice distortion. The majority of the grains show little to no internal lattice distortion except when clustered (Fig. 9C–F). Lattice distortion within individual grains ranges from <1° (Fig. 9Ci) to ~5° (Fig. 9Cii, G, H). If Type 2 grains are clustered, one or two of them will show some lattice distortion with rotations consistent with the activation of the (100)<001 > slip system (Fig. 9D).

5. Discussion

5.1. Microstructural record of local and external melt signatures within a metapelitic migmatite

Microstructural analysis of the different domains within SH2009 identified diagnostic microstructures indicating a multistage, melt bearing evolution for the sample. The host *Grt-Bt domain* represents the earliest assemblages within the sample. It contains the primary foliation that is crosscut by other domains and wraps around garnet porphyroblasts within the host. Within the host *Grt-Bt domain* a number of microstructures indicative of the previous presence of partial melt are observed: quartz grains with low dihedral angles with biotite, blebs of quartz in biotite and quartz with convex grain boundaries indicative of infilling (Fig. 3D–F) (Daczko and Piazolo, 2022; Holness et al., 2011; Holness and Sawyer, 2008; Lee et al., 2018). Additionally, within garnet fragments towards the rim of original grains, rare polymineralic inclusions can be found which are interpreted as melt inclusions (Cesare et al., 2009) (Fig. 3E).

The *Plag-Qtz domain* cross cuts the foliation within the host *Grt-Bt domain* at a low angle (Fig. 2B) and correlates with the plagioclase-quartz dominated leucosomes observed in the outcrop. Melt related microstructures are found within this domain including plagioclase grains with low dihedral angles and 'string of beads' textures (Fig. 3G), rounded, irregular coarse plagioclase (Figs. 2B, 3G, H) interpreted as xenocrystic to the host as well as a high abundance of accessory minerals including zircon. The lack of any reaction textures between the *Plag-Qtz domain* and the host likely indicates that these leucosomes represent largely locally derived melt originating from partial melting of the host *Grt-Bt domain* (Carvalho et al., 2016; Daczko and Piazolo, 2022; Gardner et al., 2020; Meek et al., 2019; Piazolo et al., 2020; Stuart et al., 2017).

Even though the *Plag-Qtz-Ky domain* is visually quite different from the *Plag-Qtz domain* it also has an abundance of microstructures that indicate the former presence of melt. Myrmekite is abundant in addition to highly elongate quartz grains with low dihedral angles and quartz at triple junctions with geometries typical for former interstitial melt (Fig. 3I–Jii) (Daczko and Piazolo, 2022). Unlike the *Plag-Qtz domain* we infer that the melt in this domain has been externally derived, based on reaction features of this domain with the other domains. This will be discussed in greater detail in a dedicated section below.

Based on microstructural analysis SH2009 shows evidence for former presence of melt within all domains. We interpret melt microstructure within the *Grt-Bt* and the *Plag-Qtz domains* to be directly related to each other, where in-situ partial melting within the *Grt-Bt domain* leads to local melt accumulation forming the *Plag-Qtz domain*. In contrast, the *Plag-Qtz-Ky domain* is ascribed to externally derived melt, migrating through the sample. None of the domains contains K-feldspar, indicating fluid-present melting throughout the sample evolution (Dyck et al., 2020).

5.2. Kyanite morphology allows in-depth understanding of its petrological association in terms of growth relative to melt generation and crystallization

Type 1 kyanite is restricted to within the host *Grt-Bt domain*, in association with garnet and/or biotite. No kyanite inclusions are present within the garnet porphyroblasts, however, inclusions of garnet are rarely found within Type 1 kyanite (Figs. 3B, 6D), indicating that kyanite grew *syn*- to post-garnet in the mineral paragenesis. Sillimanite is seen to grow syn- to post-garnet by being present as inclusions and in the matrix surrounding garnet porphyroblasts (Fig. 2B). Kyanite grows after sillimanite as rare sillimanite inclusions are found in Type 1 kyanite, further strengthening the timing of Type 1 kyanite growth. The inclusions of biotite, rutile, ilmenite, quartz and plagioclase indicate an early assemblage of garnet, biotite, plagioclase, rutile, ilmenite, sillimanite and quartz before and during Type 1 kyanite growth (Fig. 4Cii, 6E). Observed oscillatory zoning which aligns with the crystal facets (Fig. 4Aii), is interpreted to suggest melt presence during growth (Vernon, 2011; Yardley et al., 1991). In combination with the presence of melt related microstructures within the host *Grt-Bt domain* (Fig. 3D–F), Type 1 kyanite is interpreted to have grown in the presence of partial melt during the prograde to peak stage of the metamorphic evolution.

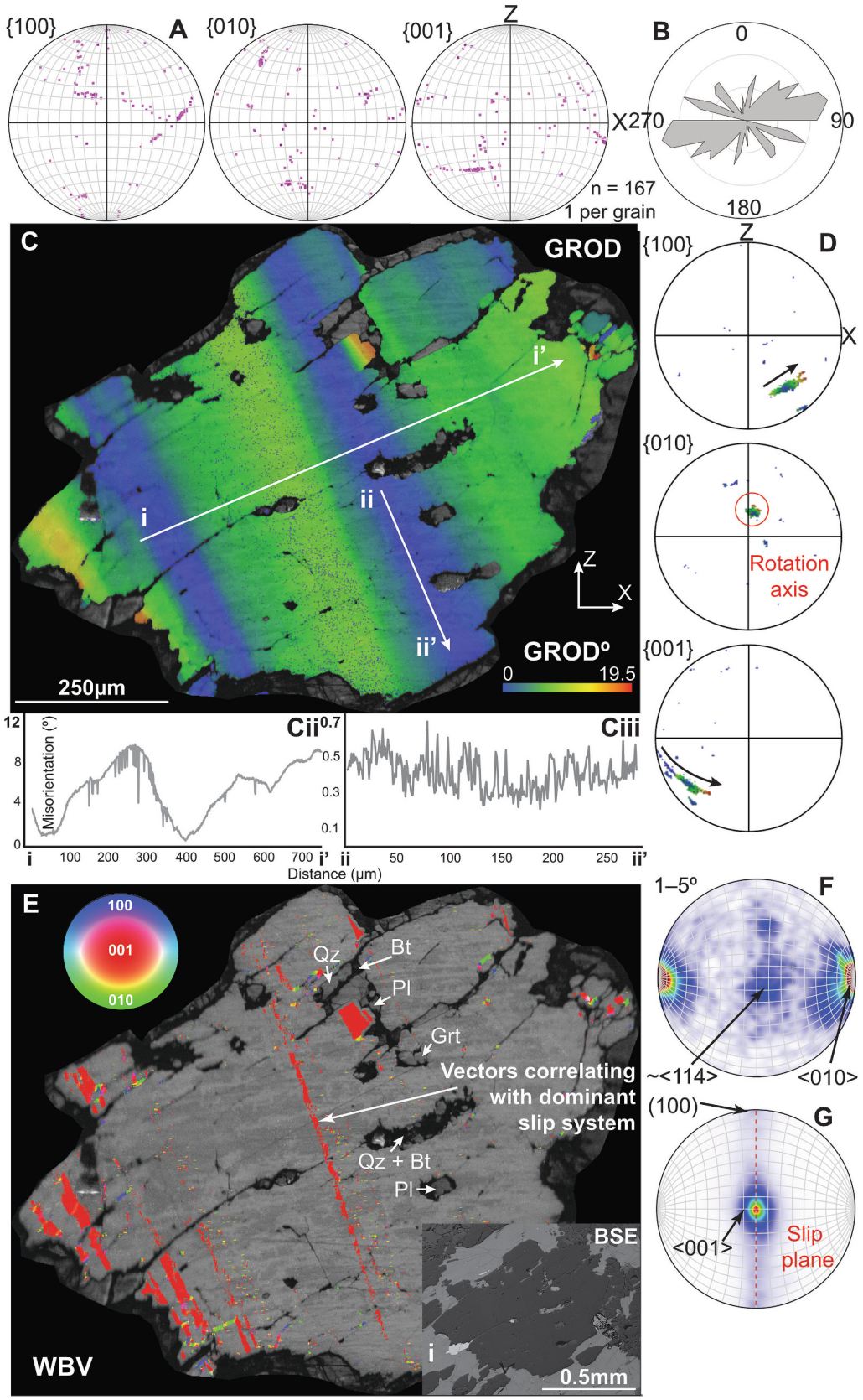

(caption on next page)

Fig. 6. Type 1 bent kyanite EBSD data. A) Upper hemisphere pole figures (equal area), plotted as one point per crystallite, displaying a weak CPO. B) Rose diagram showing a moderate SPO. C) Grain Reference Orientation Deviation (GROD) EBSD map with a band contrast map underlay showing deformation bands correlating with undulose extinction. Cii) Misorientation profile perpendicular to deformation bands. Ciii) Misorientation profile parallel to a deformation band. D) Upper hemisphere pole figures (equal area) of a single grain displaying with a cluster of data around {010} and systematically dispersed data in {100} and {001}, colour coded by GROD angle. E) Weighted Burger Vector (WBV) map with each vector colour coded by Inverse Pole Figure (IPF) colours and band contrast map underlay. Red WBV's, along {010}, correlate with the regions next to areas with low GROD angle. F) Low angle misorientation axes plotted in crystal coordinates, the bulk of the data correlates with a rotation axis around <010>. G) WBV's plotted in crystal coordinates, indicating slip direction and slip plane of the dominant slip system. (For interpretation of the references to colour in this figure legend, the reader is referred to the web version of this article.)

This interpretation is consistent with the fact that Type 1 kyanite is coarse grained indicating that nucleation was comparatively difficult (Ague and Carlson, 2013).

The most common prograde kyanite forming reactions involve the breakdown of mica (mostly muscovite but potentially biotite) (Phillips et al., 2023) and staurolite (McLellan, 1985) along with in-situ melt generation. No staurolite relics have been found. While there is muscovite within the sample it is all texturally late and not present as inclusions. Even though there is still biotite present in the sample, a partial melting reaction which shifts the modal percentages of biotite is possible. All of the melt related microstructures identified within the sample involve biotite (Fig. 3D–F), therefore we suggest that Type 1 kyanite grew during partial melting involving consumption of biotite though we cannot rule out a muscovite-based reaction. As the sample is quite hydrous this likely occurred at the lower end of metapelitic solidus temperatures around ~650–750 °C.

Restricted to within the *Plag-Qtz-Ky domain*, Type 2 kyanite is rimmed by a film of plagioclase and in turn by a rim of quartz (Fig. 3I–J). Similar to the plagioclase and quartz in this domain, Type 2 kyanite is consistently fine grained and abundant contrasting the relatively low number of large, generally non-clustered Type 1 grains (Fig. 2B). Different to Type 1 grains no inclusions are present within Type 2 grains. All of these features indicate that when Type 2 kyanite grew nucleation was much easier. Similar to Type 1 kyanite, Type 2 kyanite also contains subtle oscillatory zoning (Fig. 4D, E). When coupled with the plagioclase and quartz films as well as other microstructures within the *Plag-Qtz-Ky domain*, that indicate former presence of melt, Type 2 kyanite is interpreted to have nucleated directly from a melt during slow melt crystallization supporting high nucleation rates (Roselle et al., 1997).

5.3. Dominant deformation mechanisms in kyanite link to differences in petrological evolution

Based on EBSD analysis, Type 1 kyanite underwent progressive deformation in a locally high stress regime. Type 1 kyanite records systematic deformation resulting in well-defined deformation bands through the activation of the (100)<001 > slip system (Figs. 6F, G, 9), which has been reported to be effectively the sole slip system acting within kyanite both in natural rocks (Beane and Field, 2007; Lenze et al., 2005; Peterman et al., 2021) and experimental products (Boland et al., 1977; Kerrick, 1986; Menard et al., 1979; Raleigh, 1965). We also see some input from (001)<100> (Figs. 6D,G, 7B,F). The presence of low angle sub-grain boundaries is interpreted to be consistent with dislocation climb (Fig. 7A), particularly where areas adjacent to a subgrain boundary are flat in terms of misorientation (Fig. 7Aii). In this case, recovery must have taken place which necessitates climb (e.g. Borthwick and Piazolo, 2010). The observed features suggest the activity of dislocation climb (e.g. Carrez et al., 2024 and references within) along with dislocation glide as suggested by grains characterized by lattice bending without subgrain formation (Fig. 6). It should be noted that kyanite has a dominant parting cleavage along {100} (Deer et al., 2013). This cleavage is at high angles to crystal bending and parallel to the slip plane of the main activated slip system. As such, we cannot exclude some component of cleavage parallel gliding.

Some Type 1 grains display well defined twinning (Fig. 7). We interpret these twins to represent deformation rather than growth twins based on their slight tapering along the length of each twin (Fig. 7A*). Twins are highly systematic in their crystallographic relationships which rules them out as potentially being kink bands which are broader, less systematic in their crystallographic relationships and typically exhibit a displacement along the kink band. Unlike kink bands, there is limited previous work on the systematics of twinning in kyanite except a few works based on natural samples and experiments (Boland et al., 1977; Lefebvre and Menard, 1981). In Type 1 kyanite the twins occur with ~180° of rotation around <−10–4 > and twin plane of (100) (Fig. 7A). The twin plane we identify is similar to that reported by Boland et al. (1977) and the α twin of Lefebvre and Menard (1981).

The occurrence of these deformation features likely occurred through progressive deformation, with strain hardening triggering the activation of additional slip systems and modes of deformation. Since the twinning shows some passive bending induced by the two main activated slip systems, we interpret twinning to occur early in the deformation in accordance to the general observations that twins are responses to locally high stresses at relatively low temperatures (e.g. Lacombe et al., 2021 and references therein). The locally high stresses necessary to induce the observed deformation features at the grain scale, suggest that the sample retained a relatively strong crystal framework during deformation even though melt was present. At lower melt volumes, the influence of local high stresses is higher. The plastic deformation recorded within Type 1 kyanite, which has been shown to have a relationship with early partial melting, indicates therefore that the volume of partial melt at any one time within the *Grt-Bt domain* was, within the grain boundary network, low (Gleason et al., 1999; Hirth and Kohlstedt, 1995a, 1995b; Mei et al., 2002; Walte et al., 2005). This correlates well with the prograde to peak timing of the Type 1 kyanite suggested by petrological observations, and supports kyanite formation from mica dehydration melting (e.g. Fig. 3, cf. section above). The weak to moderate bulk CPO and SPO of the Type 1 kyanite (Fig. 6A, B) cannot be explained by crystal plastic deformation alone but suggests a degree of stress-controlled growth and minor rigid body rotation.

Unlike Type 1, Type 2 kyanite shows comparatively little internal crystal plastic deformation. Where plastic deformation does occur, albeit at a significantly lower magnitude, it does record the same dominant (100)<001> slip system, although it is less distinct (Fig. 9F). Importantly, such crystal plastic deformation is only observed in grains that occur in clusters (Fig. 9C). We therefore conclude that crystal plastic deformation was only induced where grains of kyanite impinged each other causing locally relatively high stresses at the grain scale. Type 2 kyanite shows a strong SPO with a relatively weak-moderate CPO (Fig. 9B (SPO), Fig. 9A (CPO)). The limited nature of internal deformation coupled with strong SPO implies the action of rigid body rotation in a flowing melt layer similar to that seen within flowing igneous rocks (Zibra et al., 2012). A strong SPO suggests flow occurred likely in a transpressive regime (e.g. Piazolo et al., 2002). The apparent CPO is a result of the strong SPO where the long shape axis correlated with the X axis (Fig. 9C). To allow for a significant amount of rigid body rotation and low internal deformation the ratio of flowing viscous matrix to rigid crystal must have been high (e.g. Biermeier et al., 2001). The necessary larger volume of melt forming an interconnected fluid network is supported by ubiquitous melt-related microstructures within the *Plag-Qtz-Ky domain* as well as the crystallization of the Type 2 kyanite from the melt where it is easier to nucleate.

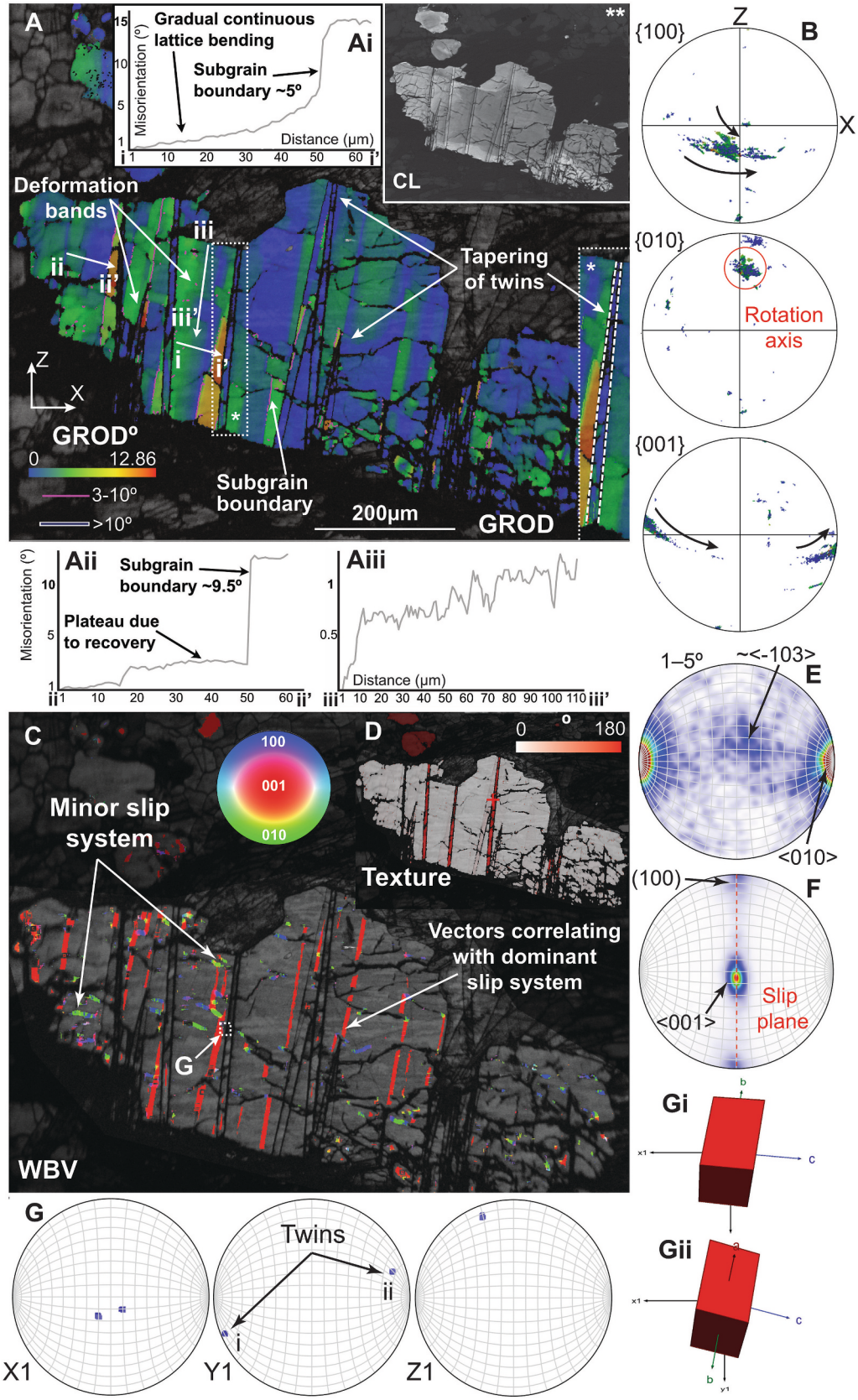

(caption on next page)

Fig. 7. Type 1 twinned kyanite EBSD data. A) GROD EBSD map with band contrast underlay showing deformation bands oblique to sharply defined twins. *) Zoomed in area highlighting the tapering of twins, **) CL image of the same grain. Ai–iii) Misorientation profiles. B) Upper hemisphere pole figures (equal area) of the grains in 7 A displaying a cluster of data around {010} and systematically dispersed data along the great circle in {100} and {001}, colour coded by GROD angle. C) WBV map with each vector colour coded by IPF colours and band contrast map underlay. Red WBV's, along {010}, correlate with the oblique deformation bands. D) Texture Component map highlighting the twins within this grain in red, bright red cross is the selected reference point. E) Low angle misorientation axes plotted in crystal coordinates, the bulk of the data correlates with a rotation axis around <010>. F) WBV's plotted in crystal coordinates, indicating slip direction and slip plane of the dominant slip system. G) Inverse pole figure of a kyanite twin (area G in 7C), data in this pole figure is at 0.2 μm resolution. Gi-Gii) Unit cell for each side of the twin plane. (For interpretation of the references to colour in this figure legend, the reader is referred to the web version of this article.)

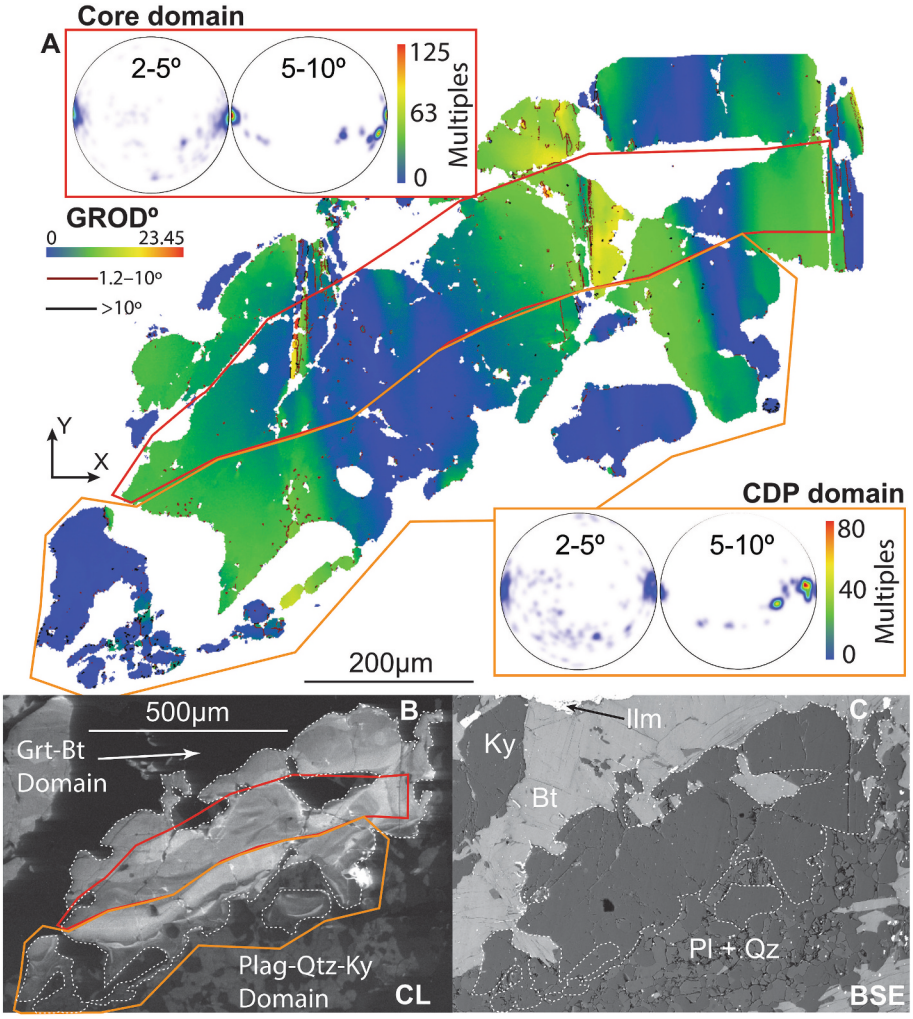

Fig. 8. Variation in microstructural signature between Type 1 kyanite cores (red) and high CL response lobate regions + dark outer rims (orange). A) GROD map and inverse pole figures plotting low angle misorientations in Crystal Coordinates. Half width of 5.0°. Low angle grain boundaries are delineated in dark red. B—C) Related CL and BSE image of these kyanite grain showing lobate outer region and dark rim and moderate grey CL core in proximity to plagioclase + quartz melt pseudomorph. A zoomed in image of same area is available in Fig. 4B as well as location of trace map in 5G-I. (For interpretation of the references to colour in this figure legend, the reader is referred to the web version of this article.)

5.4. Trace elements and CL patterns in kyanite provide insight into mechanisms of growth and melt-mediated interface-coupled dissolution-precipitation reactions

Whilst deformation and petrological information from kyanite provide a lot of insight into the evolution of this sample, further insight into the mechanisms of growth and elemental modifications can be gathered through careful analysis of internal zoning via CL and trace element maps. Type 1 kyanite cores show a moderate grey CL response which correlates with moderate concentrations of both Cr and V (e.g. Fig. 4A and Fig. 5J, K; Figs. 4B and 5D, F). A similar correlation has been observed for kyanite previously (Müller et al., 2003; Peterman et al., 2021; Phillips et al., 2023). The geometry of the observed oscillatory zoning in the cores is crystallographically defined as these zones align with the crystal facets (Fig. 4Aii). By being aligned with the crystal facets this zoning is interpreted to be primary as opposed to being potentially inherited from previous mineral microstructures like mica-rich regions that has been interpreted to be possible by Peterman et al. (2021). The trace elements in kyanite in general (Fig. 5) could be sourced from the melt, though the partitioning of Cr and V is not well constrained in all melt types. Alternatively, partitioning between different accessory phases may be invoked to explain trace element signatures. Ilmenite and rutile are present within the host *Grt-Bt domain* as well as the locally sourced *Plag-Qtz domain* which can partition Cr and V as trace elements (Kotowski et al., 2021). Ilmenite and rutile may have buffered the amount of Cr and V available to kyanite which was growing syn to post

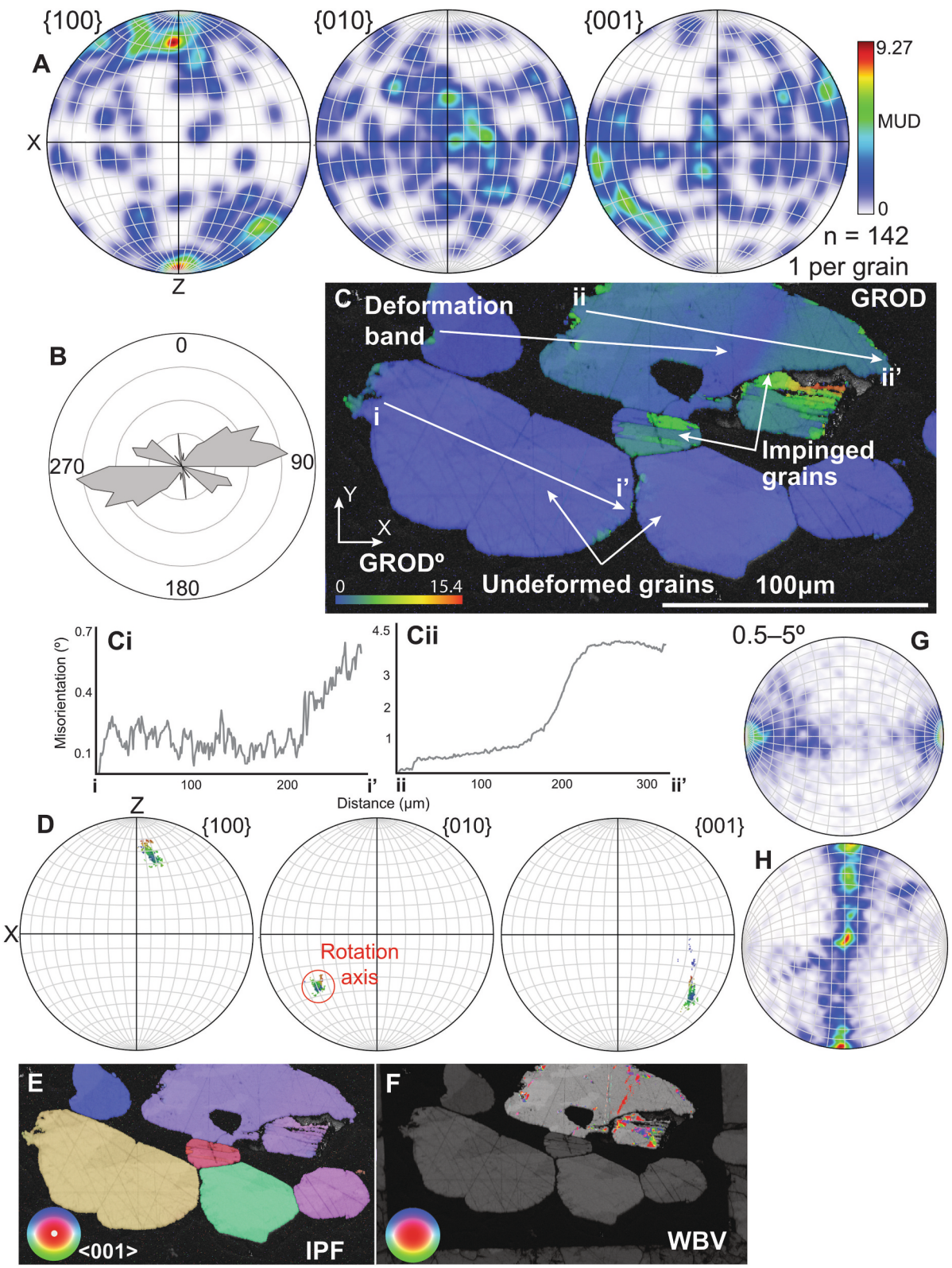

Fig. 9. Type 2 kyanite EBSD data. A) Contoured upper hemisphere pole figures (equal area), plotted as one point per crystallite/grain, displaying a weak-moderate CPO. B) Rose diagram showing a strong SPO. C) Example of some Type 2 kyanites (correlating with Fig. 3F) showing little to no internal deformation, with rare grains showing impingement and the same (100)<001 > related bending. Ci) Misorientation profile in effectively undeformed grain. Cii) Misorientation profile within a deformed grain. D) Upper hemisphere pole figures (equal area) displaying a cluster of data around {010} and systematically dispersed data along the great circle in {100} and {001}, colour coded by GROD angle. E) Type 2 kyanite grains colour coded by IPF colours. F) WBV map with each vector colour coded by IPF colours and band contrast map underlay, some artifact vectors along scratches seen in band contrast but dominant vectors correlate with rare deformation bands. G) Low angle misorientation axes plotted in crystal coordinates. The data has been filtered so that there are no artifacts from scratches. The bulk of the data correlates with a rotation axis around <010>. H) WBV's plotted in crystal coordinates, high degree of noise but there is a cluster similar to Figs. 6G and 7F. (For interpretation of the references to colour in this figure legend, the reader is referred to the web version of this article.)

ilmenite and rutile (Type 1) as shown by presence of these minerals as inclusions in kyanite (Fig. 4Aiii, Cii). As the zoning in all kyanite is based on trace elements not major elements it is potentially highly dynamic where local subtle changes in chemistry cause oscillatory zoning, supporting the importance of heterogeneous, low melt fractions early in the metamorphic evolution.

Type 1 kyanite grains also show evidence of later modification that cross cuts and embays the cores (Fig. 4B, C). These lobate, bright CL response to dark CL response zones appear similar to features often seen in monazite (Blereau et al., 2016; Harlov et al., 2011). These zones are asymmetric and irregular in terms of their CL response but also their trace elements (Stuart et al., 2016). These zones contain increased trace element concentrations with both normal (Fig. 5C, F) and reverse zoning (Fig. 5I) potentially within a single zone. Multiple occurrences of these zones can also occur, truncating an earlier zone (Fig. 5F) indicating a highly dynamic system. EBSD analysis of the core regions versus the modified regions shows relatively more dispersion to misorientation axes and a lack of sub-grain boundaries despite being at the edges of grains within the modified regions (Fig. 8A). These changes provide additional evidence that the process forming these zones involves mineral replacement. A critical observation is that this modification is texturally restricted to grains in contact or nearby to the *Plag-Qtz-Ky domain*. The combination of these features is interpreted to be the result of melt-mediated interface-coupled dissolution-precipitation (CDP) (c.f. Fougerouse et al., 2024). During this process, melt that is in chemical disequilibrium with Type 1 kyanite dissolves the pre-existing kyanite grains at the melt-crystal interface. Dissolution of the original kyanite results in local oversaturation, triggering precipitation of a kyanite with different chemical make-up but similar crystallographic orientation. Mixing of local composition with melt reservoir provides alternative trace element chemistry for the newly precipitated kyanite. This dissolution precipitation replacement reaction occurs at a sharp reacting interface. Variations in dissolution rates as well as heterogeneous availability of the melt result in a sharp, but irregularly shaped interface crosscutting former chemical zonations (e.g. Fig. 5A, C). We suggest that this process is not singular to our samples but that for example the non-lobate high Cr rims on kyanite by Phillips et al. (2023) originated by this process rather than direct overgrowth from a melt. The fact that the trace element concentration is changing within these features indicates that the partial melt within the *Plag-Qtz-Ky domain* is not in equilibrium with the earlier generation of Type 1, implying that it is likely externally derived. This matches well with the different microstructural appearance of the *Plag-Qtz-Ky domain* as well as the little to complete lack of ilmenite and rutile that are present in the other domains.

Type 2 kyanite grains are different from Type 1 not only in terms of deformation features but also in terms of their CL response and trace element concentrations. They are consistently dark in CL response and low in trace element concentration (Figs. 4D, E and 5L–N). This combination of features is very similar, however, to the outermost irregular rims that grow on the most heavily CDP modified grains (Figs. 4B, C and 5G–I). Based on this match in both CL response and trace element concentration we interpret the Type 2 kyanite to be co-genetic with the rims forming through CDP within the host *Grt-Bt domain*. The *Plag-Qtz-Ky domain* does not have any obvious sources or sinks for Cr and V which could also explain the relatively low concentration of these elements in this population.

5.5. Crystal plastic deformation does not modify chemical signatures in kyanite

As noted in previous studies, kyanite can preserve zoning related to trace elements despite modification to the crystal lattice via kinking, bending through dislocation glide and/or twinning in locally high stress situations. Based on our study and the observations of previous studies, kyanite zoning is apparently unaffected by deformation induced diffusion. This is a highly important observation as most silicate minerals are affected by presence and movement of dislocations (e.g. zircon (e.g. Piazolo et al., 2016, 2012), pyroxene (e.g. Lund et al., 2006), titanite (e.g. Corvò et al., 2023)).

This is particularly interesting, as features such as recovered subgrains and subgrain boundaries reaching up to 10° misorientation (Fig. 7Aii) suggest that not only dislocation glide but also dislocation climb occurred. Dislocation climb necessitates diffusion and dislocation movement, hence its activity is expected to have a significant effect on elemental redistribution (e.g. Piazolo et al., 2016) including major elements (e.g. Al, Si and O in kyanite). As such, the underlying reason why the trace element signature and zoning is preserved despite the activity of dislocation glide and climb, is not entirely clear. If the trace elements are incorporated via substitution, likely coupled substitution as Cr and V are high valence ions, then dislocations acquired through deformation would not be able to modify the trace elements easily. Trace elements would not be able to move through pipe diffusion along subgrain boundaries in this case. If the trace elements were located interstitially then we would expect more modification as they would be in a higher energy configuration. As such interstitial trace elements would be expected to be attracted to moving dislocations allowing enhanced diffusion plus potential diffusion along subgrain boundaries (Piazolo et al., 2016). One possibility is that the deformation within kyanite occurs so ‘perfectly’ that diffusional processes related to dislocations do not get to occur. Kyanite is known for having near perfect stacking faults (Lefebvre and Menard, 1981), and these stacking faults do not modify any cationic polyhedra (Kerrick, 1986). Additionally, the deformation twinning within kyanite also does not require any additional atomic shuffle which could result in planes of fast pipe diffusion (e.g. Piazolo et al., 2016). One further mechanism to consider is through the recently reported structural feature of ripplocations. Ripplocations are a buckling phenomenon that occurs in the basal layers of layered solids (in particular within kinking nonlinear elastic solids) and are interpreted to be connected to the formation of kink bands and explain c-axis strain (Gruber et al., 2016; Plummer et al., 2021). Unlike dislocations, ripplocations have no Burgers vector and attract each other, in similar elastic atomic folds/waves (Gruber et al., 2016). Ripplocations permit glide to occur without changing the overall structure of the crystal lattice and do not require the breaking of in-plane bonds (Aslin et al., 2019). Due to the lack of and/or movement of lattice defects/vacancies, the formation of ripplocations removes the increased opportunity for diffusion that dislocations provide as the lattice is being warped elastically. As kyanite has quite a strong cleavage and generally layered structure to individual crystals it is possible that ripplocations may occur within this mineral, though a future study will be needed to investigate this possibility in more detail.

In contrast, replacement reactions will, by their nature of local dissolution and precipitation out of a chemically different fluid, readily change the trace element signature of kyanite. Consequently, kyanite within samples bearing fluids should be highly scrutinised with multi-disciplinary analysis, regardless of the degree of deformation, to gain insight into the sample evolution and fluid processes.

5.6. Kyanite and the metamorphic evolution of South Harris

Previous studies in the south of the Leverburgh belt within South Harris have interpreted an ultra-high temperature (UHT) anticlockwise *P–T* evolution (Baba, 1998; Baba, 1999; Baba, 2003; Baba, 2004; Baba et al., 2012; Hollis et al., 2006). This *P–T* evolution was defined from combining information from garnet-kyanite and orthopyroxene-garnet-kyanite gneisses and sapphirine-bearing garnet-kyanite granulites within the Benn Obbe and Rodel Series of the Leverburgh belt (Baba, 1998, Baba, 1999, Baba, 2003, Baba, 2004, Baba et al., 2012, Hollis et al., 2006).

At present the exact conditions of metamorphism are not definable for our sample. Our sample is defined by disequilibrium assemblages allowing the preservation of all three aluminosiliates with little to no

sequential replacement but because of this contains a host of information that may not be present in an equilibrated sample that would be ideal for phase equilibria. Hence, this study focuses on other means of constraining the metamorphic evolution of this unique sample. The *P–T–t* evolution will be the focus of a future investigation. From our analysis of the sample, we interpret the mineral paragenesis to define an anticlockwise evolution (sillimanite ➔ kyanite ➔ andalusite), this will be further assessed in a future study. Therefore, the style of metamorphism recorded by our sample is likely similar to previous studies in the south. It is possible however, that the more northern extension of the Leverburgh belt experienced different conditions of metamorphism based on the current lack of UHT indicator minerals. Additionally, no traditional *P–T* studies exist within the Chaipaval Pelitic Series where our sample resides so this could also be a potential explanation for different conditions. Future studies should assess the difference in conditions north to south and between series.

5.7. *Kyanite as a powerful petrological tool to decipher tectonometamorphic evolution of high-grade rocks*

We propose the following model for the evolution of the studied migmatite which is closely linked to the evolving characteristics of the observed two types of kyanite (Fig. 10).

In Stage 1 during prograde metamorphism (Fig. 10A), garnet cores grow within the *Grt-Bt* host *domain* consistent with the metamorphic *P–T* path of Baba (2004) and Hollis et al. (2006) during solid state metamorphism. Progressive increase in temperature and pressure during deformation results in the formation of the primary S1 fabric, local partial melting and further growth of garnet rims during this period (Fig. 10A). During growth, garnet entraps melt in its rim as well as aligned sillimanite laths. During the later part of Stage 1, Type 1 kyanite nucleates within the *Grt-Bt domain* as part of the partial melt reaction resulting in oscillatory zoning (Fig. 11A). At any point in time, there is a low melt volume present in the rock matrix. Consequently, progressive deformation of existing Type 1 kyanite by dislocation creep and twinning occurs while partial melting is still ongoing locally (Fig. 11B).

In Stage 2 (Fig. 10B), two different melt related processes occur:

1) melting in adjacent lithologies expels melt and this externally derived, chemically distinct melt infiltrates the *Grt-Bt domain* of the studied sample. This externally derived melt reacts with Type 1 kyanite within the *Grt-Bt domain*, if physically in contact. Due to the chemical differences, melt-mediated interface coupled dissolution precipitation (CDP) results in the local, partial replacement of Type 1 kyanite by kyanite of distinctly different trace element composition and thus CL signature (Fig. 11C). The melt initiating CDP of Type 1 kyanite is the same externally derived melt within which a high number of small Type 2 kyanite nucleate. This melt is chemically distinct compared to the trace element poor melt during initial melt crystallization with minor oscillatory zoning and dark CL signatures (Fig. 11D). Continued deformation during this stage results in rigid body rotation of the kyanite grains causing SPO and CPO with minimum crystal plastic deformation (Fig. 11E). This low degree of crystal plastic deformation suggests high melt to crystal load ratios. Late-stage crystallization of the externally derived melt results in the formation of *Plag-Qtz-Ky domain* as plagioclase and quartz crystallize out (Fig. 11F).
2) ongoing deformation aids self-organization of the in-situ, locally produced partial melt into areas of high melt volume that then become mobile, causing a cross-cutting leucosome network recognised as the *Plag-Qtz domain* (e.g. Weinberg et al., 2015) (Fig. 10B). Kyanite helps define a suprasolidus anti-clockwise *P–T* path at

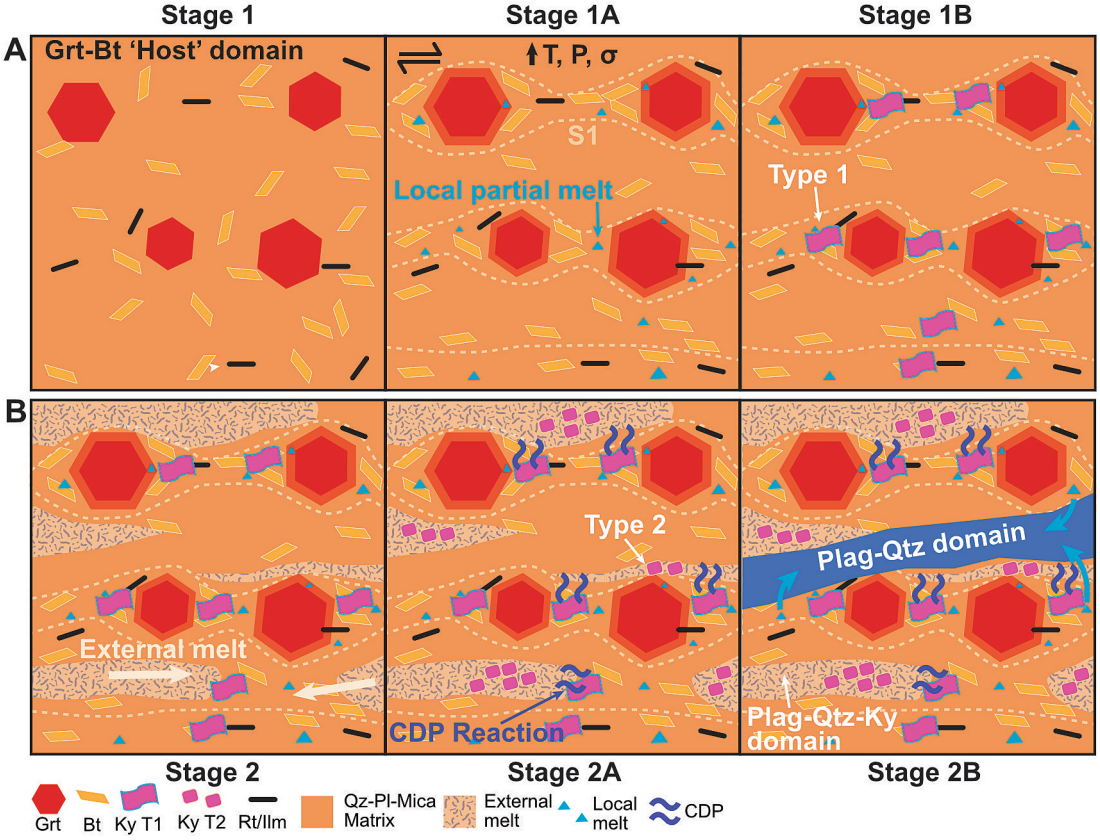

Fig. 10. Texture model for the evolution of SH2009. Stage 1 – Garnet core growth in a generic Qtz-Plag-mica matrix; 1 A – S1 fabric formation, garnet rim growth and onset of partial melting; 1B –Type 1 kyanite nucleation in the presence of partial melt; Stage 2 – External melt is introduced; 2 A – Melt-related CDP reactions occur to Type 1 kyanite and nucleation of Type 2 kyanite. 2B – Transfer of local partial melt to form the *Plag-Qtz domain*.

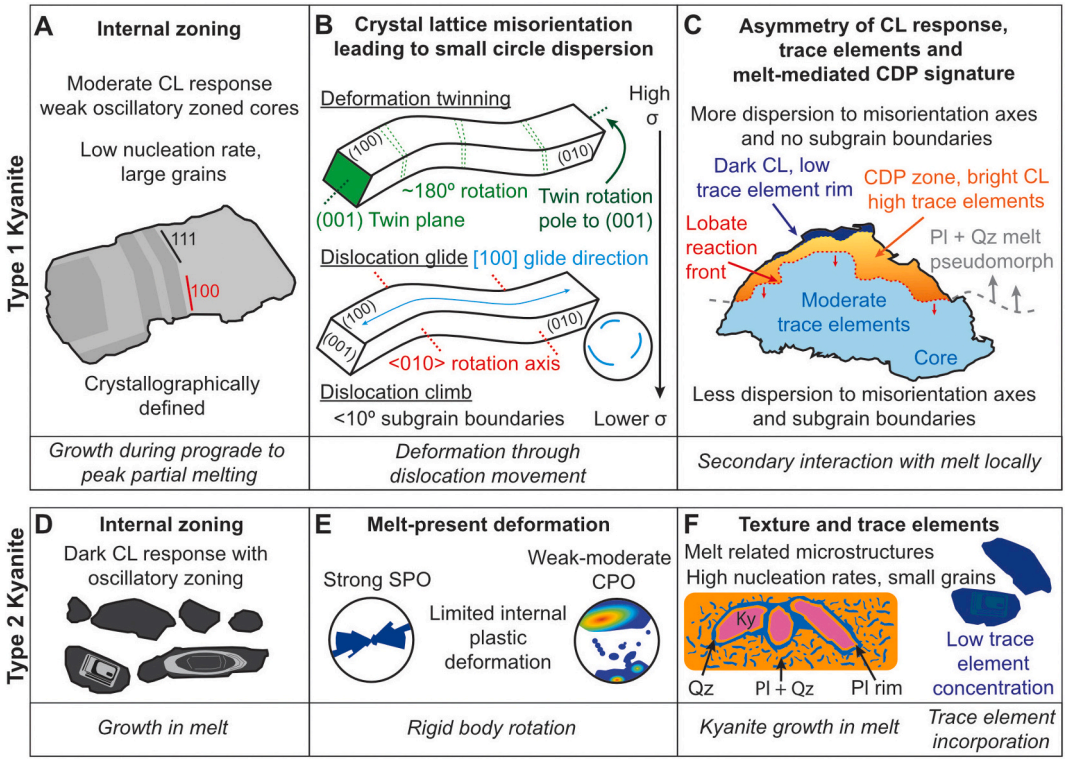

Fig. 11. Summary figure of the features, observations (bold) and processes (italic) effecting and defining Type 1 and Type 2 kyanite; see text for more details.

granulite facies conditions, contrasting to the conditions reported elsewhere in South Harris.

Our model highlights that kyanite can not only provide information regarding *P–T* conditions experienced by a sample but with careful analysis, many more layers of information can be unravelled. By imaging and classifying CL zoning, and mapping trace element distribution we can interrogate the processes through which the kyanite grew as well as identify different populations (Figs. 10 and 11). By combining all of this information, independent of *P–T* estimates, kyanite can provide a very detailed multi-stage picture of the tectono-metamorphic evolution of high-grade and partially melted rocks. We highlight here specific characteristics of kyanite and their potential use as a petro-structural tool (Fig. 11):

- Oscillatory trace element zoning and CL signatures suggest growth in the presence of melt. If grains are large, nucleation was difficult suggesting prograde reaction and low melt percentages supporting kyanite formation during partial melting (e.g. Type 1 kyanite, Fig. 11A).
- Kyanite crystal plastic deformation features such as continuous bending, subgrain boundaries and deformation twinning allow the deciphering of the temporal relationship between growth and deformation as well as for the inference of related stress levels (e.g. Type 1 kyanite, Fig. 11B).
- Asymmetric areas of different CL and trace element signatures within grains that are sharp and irregular in shape, and truncate pre-existing signatures are tell tales of fluid mediated interface coupled dissolution-replacement reactions. These not only modify the chemical make-up but also the crystallographic signatures (e.g. Type 1 kyanite, Fig. 11C).
- Differences in intensity of CL signatures can be used to distinguish different chemical environments of growth (e.g. Type 1 versus Type 2 kyanite, Fig. 11D).
- The coincidence of SPO and CPO of a population of kyanite with limited internal crystal plastic deformation features within individual grains suggests melt present deformation by rigid body rotation in an environment of high melt to crystal volume ratio (e.g. Type 2 kyanite, Fig. 11E).
- Kyanite grains with asymmetric rims of quartz/plagioclase may indicate growth directly out of a melt. In this case, high nucleation rates are common resulting in numerous, small grains (e.g. Type 2 kyanite, Fig. 11F).

The use of kyanite as a petro-structural tool could be consolidated by the construction of a deformation mechanism map for solid state deformation allowing quantitative interpretation of deformation structures. In addition, presently there is no partitioning information for trace elements in kyanite with melt, major minerals such as garnet or accessory minerals such as rutile. With this additional information kyanite could become an indispensable tool just like other minerals that are common targets of multidisciplinary analysis (e.g. zircon, garnet, rutile).

6. Conclusions

This study shows that kyanite has the potential to be highly sensitive to changes in partial melt composition, volume and deformation during tectono-metamorphic events. In a garnet-biotite bearing migmatite from South Harris, NW Scotland, we identified two discrete generations of kyanite that can be distinguished through correlative and multidisciplinary analysis. Type 1 kyanite grew *syn-* to post-garnet growth when a low volume of partial melt was present based on petrology, CL textures and progressive deformation information. Type 1 kyanite underwent locally melt-mediated interface-coupled dissolution precipitation where Type 1 grains are in contact with the *Plag-Qtz-Ky domain* resulting in modified trace elements and textures. Type 2 kyanite grew within this domain and later underwent rigid body rotation through melt-present deformation within a larger volume of melt. This melt was externally derived, transgressed the gneiss, and resulted in the local CDP of Type 1

which was co-genetic with Type 2 growth, resulting in similar trace elements and CL response. This study highlights that through detailed multidisciplinary analysis kyanite is a petrological toolbox capable of unravelling metamorphic and deformational events within high-grade and partially melted rocks.

CRediT authorship contribution statement

Eleanore Blereau: Conceptualization, Data curation, Formal analysis, Funding acquisition, Investigation, Methodology, Project administration, Validation, Visualization, Writing – original draft, Writing – review & editing, Resources. **Sandra Piazolo:** Conceptualization, Data curation, Formal analysis, Funding acquisition, Investigation, Methodology, Project administration, Validation, Visualization, Writing – original draft, Writing – review & editing, Resources. **Patrick Trimby:** Data curation, Investigation, Methodology, Writing – review & editing. **Etienne Skrzypek:** Data curation, Writing – review & editing.

Declaration of competing interest

The authors have no conflicts of interest to declare.

Acknowledgements

We thank Alberto Ceccato and an anonymous reviewer for their feedback and constructive suggestions during the review process.

This project has received funding from the European Union's Horizon 2020 research and innovation program under the Marie Skłodowska-Curie Action grant agreement No 101018037 to E. Blereau and S. Piazolo. Thank you to R. Walshaw for his assistance with EPMA at the University of Leeds.

References

Ague, J.J., Carlson, W.D., 2013. Metamorphism as garnet sees it: the kinetics of nucleation and growth, equilibration, and diffusional relaxation. Elements 9, 439–445.

Albee, A.L., Chodos, A.A., 1969. Minor element content of coexistent Al 2 SiO 5 polymorphs. Am. J. Sci. 267, 310–316. https://doi.org/10.2475/AJS.267.3.310.

Aslin, J., Mariani, E., Dawson, K., Barsoum, M.W., 2019. Ripplocations provide a new mechanism for the deformation of phyllosilicates in the lithosphere. Nat. Commun. 10, 686. https://doi.org/10.1038/s41467-019-08587-2.

Baba, S., 1998. Proterozoic anticlockwise P-T path of the Lewisian Complex of South Harris, Outer Hebrides, NW Scotland. J. Metamorph. Geol. 16, 819–841. https://doi.org/10.1111/J.1525-1314.1998.00163.X.

Baba, S., 1999. Sapphirine-bearing orthopyroxene-kyanite/sillimanite granulites from South Harris, NW Scotland: Evidence for Proterozoic UHT metamorphism in the Lewisian. Contrib. Mineral. Petrol. 136, 33–47. https://doi.org/10.1007/S004100050522/METRICS.

Baba, S., 2003. Two stages of sapphirine formation during prograde and retrograde metamorphism in the palaeoproterozoic lewisian complex in South Harris, NW Scotland. J. Petrol. 44, 329–354. https://doi.org/10.1093/PETROLOGY/44.2.329.

Baba, S., 2004. Palaeoproterozoic UHT metamorphism in the Lewisian complex and North Atlantic region. J. Mineral. Petrol. Sci. 99, 202–212.

Baba, S., Dunkley, D.J., Hokada, T., Horie, K., Suzuki, K., Shiraishi, K., 2012. New SHRIMP U–Pb zircon ages and CHIME monazite ages from South Harris granulites, Lewisian Complex, NW Scotland: Implications for two stages of zircon formation during Palaeoproterozoic UHT metamorphism. Precambrian Res. 200–203, 104–128. https://doi.org/10.1016/J.PRECAMRES.2012.01.013.

Beane, R.J., Field, C.K., 2007. Kyanite deformation in whiteschist of the ultrahigh-pressure metamorphic Kokchetav Massif, Kazakhstan. J. Metamorph. Geol. 25, 117–128. https://doi.org/10.1111/J.1525-1314.2007.00692.X.

Beaumont, C., Jamieson, R.A., Nguyen, M.H., Lee, B., 2001. Himalayan tectonics explained by extrusion of a low-viscosity crustal channel coupled to focused surface denudation. Nature 414 (6865 414), 738–742. https://doi.org/10.1038/414738a.

Biermeier, C., Stüwe, K., Barr, T.D., 2001. The rotation rate of cylindrical objects during simple shear. J. Struct. Geol. 23, 765–776. https://doi.org/10.1016/S0191-8141(00)00146-2.

Blereau, E., Clark, C., Taylor, R.J.M., Johnson, T.E., Fitzsimons, I.C.W., Santosh, M., 2016. Constraints on the timing and conditions of high-grade metamorphism, charnockite formation and fluid–rock interaction in the Trivandrum Block, southern India. J. Metamorph. Geol. 34, 527–549. https://doi.org/10.1111/JMG.12192.

Boland, J.N., Hobbs, B.E., McLaren, A.C., 1977. The defect structure in natural and experimentally deformed kyanite. Phys. Status Solidi A 39, 631–641. https://doi.org/10.1002/PSSA.2210390233.

Borthwick, V.E., Piazolo, S., 2010. Post-deformational annealing at the subgrain scale: Temperature dependent behaviour revealed by in-situ heating experiments on deformed single crystal halite. J. Struct. Geol. 32 (7), 982–996.

Carrez, P., Mussi, A., Cordier, P., 2024. On dislocation climb as an important deformation mechanism for planetary interiors. Annu. Rev. Earth Planet. Sci. 52.

Carvalho, B.B., Sawyer, E.W., Janasi, V.A., 2016. Crustal reworking in a shear zone: Transformation of metagranite to migmatite. J. Metamorph. Geol. 34, 237–264. https://doi.org/10.1111/jmg.12180.

Cesare, B., Ferrero, S., Salvioli-Mariani, E., Pedron, D., Cavallo, A., 2009. "Nanogranite" and glassy inclusions: The anatectic melt in migmatites and granulites. Geology 37, 627–630. https://doi.org/10.1130/G25759A.1.

Chinner, G.A., Smith, J.V., Knowles, C.R., 1969. Transition-metal contents of Al2SiO5 polymorphs. Am. J. Sci. 267, 96–113.

Corvò, S., Maino, M., Piazolo, S., Kylander-Clark, A.R.C., Orlando, A., Seno, S., Langone, A., 2023. Crystal plasticity and fluid availability govern the ability of titanite to record the age of deformation. Earth Planet. Sci. Lett. 620, 118349 https://doi.org/10.1016/j.epsl.2023.118349.

Daczko, N.R., Piazolo, S., 2022. Recognition of melferite – A rock formed in syn-deformational high-strain melt-transfer zones through sub-solidus rocks: A review and synthesis of microstructural criteria. Lithos 430–431, 106850. https://doi.org/10.1016/J.LITHOS.2022.106850.

Dearnley, R., 1963. The Lewisian complex of South Harris With some observations on the metamorphosed basic intrusions of the Outer Hebrides, Scotland. Quart. J. Geol. Soc. London 119, 243–307. https://doi.org/10.1144/gsjgs.119.1.0243.

Deer, W.A., Howie, R.A., Zussman, J., 2013. An Introduction to the Rock-Forming Minerals.

Dyck, B., Waters, D.J., St-Onge, M.R., Searle, M.P., 2020. Muscovite dehydration melting: Reaction mechanisms, microstructures, and implications for anatexis. J. Metamorph. Geol. 38, 29–52. https://doi.org/10.1111/JMG.12511.

Fougerouse, D., Geisler, T., Reddy, S.M., Aleshin, M., Martin, L., Doucet, L.S., Quadir, Z., Saxey, D., Rickard, W., 2024. Melt-mediated re-equilibration of zircon produced during meltdown of the Chernobyl reactor. Am. Mineral. 109, 8–14. https://doi.org/10.2138/am-2022-8824.

Friend, C.R.L., Kinny, P.D., 2001. A reappraisal of the Lewisian Gneiss Complex: Geochronological evidence for its tectonic assembly from disparate terranes in the Proterozoic. Contrib. Mineral. Petrol. 142, 198–218. https://doi.org/10.1007/S004100100283/METRICS.

Frost, H.J., Ashby, M.F., 1982. Deformation-mechanism Maps: The Plasticity and Creep of Metals and Ceramics, (No Title).

Gardner, R.L., Piazolo, S., Daczko, N.R., Trimby, P., 2020. Microstructures reveal multistage melt present strain localisation in mid-ocean gabbros. Lithos 366–367, 105572. https://doi.org/10.1016/J.LITHOS.2020.105572.

Ghatak, H., Gardner, R.L., Daczko, N.R., Piazolo, S., Milan, L., 2022. Oxide enrichment by syntectonic melt-rock interaction. Lithos 414–415, 106617. https://doi.org/10.1016/J.LITHOS.2022.106617.

Gleason, G.C., Bruce, V., Green, H.W., 1999. Experimental investigation of melt topology in partially molten quartzo-feldspathic aggregates under hydrostatic and non-hydrostatic stress. J. Metamorph. Geol. 17, 705–722. https://doi.org/10.1046/J.1525-1314.1999.00228.X.

Goodenough, K., Merritt, J.W., Survey, B.G., 2011. The Outer Hebrides: A Landscape Fashioned by Geology. Landscape fashioned by geology series, Scottish National Heritage.

Gruber, J., Lang, A.C., Griggs, J., Taheri, M.L., Tucker, G.J., Barsoum, M.W., 2016. Evidence for bulk ripplocations in layered solids. Sci. Rep. 6 (1 6), 1–8. https://doi.org/10.1038/srep33451.

Harlov, D.E., Wirth, R., Hetherington, C.J., 2011. Fluid-mediate partial alteration in monazite: the role of coupled dissolution-reprecipitation in element redistribution and mass transfer. Contrib. Mineral. Petrol. 162, 329–348.

Herz, N., Dutra, C.V., 1964. Geochemistry of some kyanites from brazil. Am. Mineral. 49, 1290–1305.

Hirth, G., Kohlstedt, D.L., 1995a. Experimental constraints on the dynamics of the partially molten upper mantle: 2. Deformation in the dislocation creep regime. J. Geophys. Res. Solid Earth 100, 15441–15449. https://doi.org/10.1029/95JB01292.

Hirth, G., Kohlstedt, D.L., 1995b. Experimental constraints on the dynamics of the partially molten upper mantle: Deformation in the diffusion creep regime. J. Geophys. Res. Solid Earth 100, 1981–2001. https://doi.org/10.1029/94JB02128.

Hollis, J.A., Harley, S.L., White, R.W., Clarke, G.L., 2006. Preservation of evidence for prograde metamorphism in ultrahigh-temperature, high-pressure kyanite-bearing granulites, South Harris, Scotland. J. Metamorph. Geol. 24, 263–279. https://doi.org/10.1111/J.1525-1314.2006.00636.X.

Holness, M.B., Sawyer, E.W., 2008. On the pseudomorphing of melt-filled pores during the crystallization of migmatites. J. Petrol. 49, 1343–1363. https://doi.org/10.1093/PETROLOGY/EGN028.

Holness, M.B., Cesare, B., Sawyer, E.W., 2011. Melted rocks under the microscope: microstructures and their interpretation. Elements 7, 247.

Kendrick, J., Indares, A., 2018. The reaction history of kyanite in high-P aluminous granulites. J. Metamorph. Geol. 36, 125–146. https://doi.org/10.1111/jmg.12286.

Kerrick, D.M., 1986. Dislocation strain energy in the Al2SiO5 polymorphs. Phys. Chem. Miner. 13, 221–226. https://doi.org/10.1007/BF00308272/METRICS.

Kinny, P.D., Friend, C.R.L., Love, G.J., 2005. Proposal for a terrane-based nomenclature for the Lewisian Gneiss Complex of NW Scotland. J. Geol. Soc. Lond. 162, 175–186. https://doi.org/10.1144/0016-764903-149.

Kotowski, J., Nejbert, K., Olszewska-Nejbert, D., 2021. Rutile mineral chemistry and zr-in-rutile thermometry in provenance study of albian (Uppermost lower cretaceous)

terrigenous quartz sands and sandstones in southern extra-carpathian Poland. Minerals 11, 553. https://doi.org/10.3390/MIN11060553/S1.
Lacombe, O., Parlangeau, C., Beaudoin, N.E., Amrouch, K., 2021. Calcite twin formation, measurement and use as stress–strain indicators: a review of progress over the last decade. Geosciences (Basel) 11, 445.
Lanari, P., Vidal, O., De Andrade, V., Dubacq, B., Lewin, E., Grosch, E.G., Schwartz, S., 2014. XMapTools: A MATLAB©-based program for electron microprobe X-ray image processing and geothermobarometry. Comput. Geosci. 62, 227–240. https://doi.org/10.1016/J.CAGEO.2013.08.010.
Lee, A.L., Torvela, T., Lloyd, G.E., Walker, A.M., 2018. Melt organisation and strain partitioning in the lower crust. J. Struct. Geol. 113, 188–199. https://doi.org/10.1016/j.jsg.2018.05.016.
Lefebvre, A., Menard, D., 1981. Stacking faults and twins in kyanite, Al2SiO5. Acta Crystallogr. A 37, 80–84.
Lenze, A., Stöckhert, B., Wirth, R., 2005. Grain scale deformation in ultra-high-pressure metamorphic rocks—an indicator of rapid phase transformation. Earth Planet. Sci. Lett. 229, 217–230. https://doi.org/10.1016/J.EPSL.2004.10.012.
Lund, M.D., Piazolo, S., Harley, S.L., 2006. Ultrahigh temperature deformation microstructures in felsic granulites of the Napier Complex, Antarctica. Tectonophysics 427, 133–151. https://doi.org/10.1016/j.tecto.2006.05.022.
McLellan, E., 1985. Metamorphic reactions in the kyanite and sillimanite zones of the barrovian type area. J. Petrol. 26, 789–818. https://doi.org/10.1093/petrology/26.4.789.
Meek, U., Piazolo, S., Daczko, N.R., 2019. The field and microstructural signatures of deformation-assisted melt transfer: Insights from magmatic arc lower crust, New Zealand. J. Metamorph. Geol. 37, 795–821. https://doi.org/10.1111/JMG.12488.
Mei, S., Bai, W., Hiraga, T., Kohlstedt, D.L., 2002. Influence of melt on the creep behavior of olivine–basalt aggregates under hydrous conditions. Earth Planet. Sci. Lett. 201, 491–507. https://doi.org/10.1016/S0012-821X(02)00745-8.
Menard, D., Doukhan, J.-C., Paquet, J., 1979. Uniaxial compression of kyanite Al2O3-SiO2. Bull. Mineral. 102, 159–162. https://doi.org/10.3406/BULMI.1979.7270.
Müller, A., René, M., Behr, H.J., Kronz, A., 2003. Trace elements and cathodoluminescence of igneous quartz in topaz granites from the Hub Stock (Slavkovský Les Mts., Czech Republic). Mineral. Petrol. 79 (3 79), 167–191. https://doi.org/10.1007/S00710-003-0238-3.
Neiva, A.M.R., 1984. Chromium-bearing kyanite from Mozambique. Min. Mag. 48, 563–564. https://doi.org/10.1180/minmag.1984.048.349.18.
Pearson, G.R., Shaw, D.M., 1960. Trace elements in kyanite, sillimanite and andalusite. Am. Mineral. 45, 808–817.
Peterman, E.M., Jercinovic, M.J., Beane, R.J., de Wet, C.B., 2021. Kyanite preserves prograde and retrograde metamorphic events as revealed by cathodoluminescence, geochemistry, and crystallographic orientation. J. Metamorph. Geol. 39, 843–866. https://doi.org/10.1111/JMG.12593.
Phillips, S.E., Argles, T.W., Warren, C.J., Harris, N.B.W., Kunz, B.E., 2023. Kyanite petrogenesis in migmatites: resolving melting and metamorphic signatures. Contrib. Mineral. Petrol. 178, 1–19. https://doi.org/10.1007/S00410-022-01991-W/FIGURES/9.
Piazolo, S., Austrheim, H., Whitehouse, M., 2012. Brittle-ductile microfabrics in naturally deformed zircon: Deformation mechanisms and consequences for U-Pb dating. Am. Mineral. 97 (10), 1544–1563.
Piazolo, S., Bons, P.D., Passchier, C.W., 2002. The influence of matrix rheology and vorticity on fabric development of populations of rigid objects during plane strain deformation. Tectonophysics 351, 315–329. https://doi.org/10.1016/S0040-1951(02)00220-2.
Piazolo, S., La Fontaine, A., Trimby, P., Harley, S., Yang, L., Armstrong, R., Cairney, J.M., 2016. Deformation-induced trace element redistribution in zircon revealed using atom probe tomography. Nat. Commun. 7 (1 7), 1–7. https://doi.org/10.1038/ncomms10490.
Piazolo, S., Daczko, N.R., Silva, D., Raimondo, T., 2020. Melt-present shear zones enable intracontinental orogenesis. Geology 48, 643–648. https://doi.org/10.1130/G47126.1.
Plummer, G., Rathod, H., Srivastava, A., Radovic, M., Ouisse, T., Yildizhan, M., Persson, P.O.Å., Lambrinou, K., Barsoum, M.W., Tucker, G.J., 2021. On the origin of kinking in layered crystalline solids. Mater. Today 43, 45–52. https://doi.org/10.1016/J.MATTOD.2020.11.014.
Putnis, A., 2009. Mineral replacement reactions. Rev. Mineral. Geochem. 70, 87–124.
Raleigh, C.B., 1965. Glide mechanisms in experimentally deformed minerals. Science 1979 (150), 739–741. https://doi.org/10.1126/SCIENCE.150.3697.739.
Roselle, G.T., Baumgartner, L.P., Chapman, J.A., 1997. Nucleation-dominated crystallization of forsterite in the Ubehebe Peak contact aureole, California. Geology 25 (9), 823–826.
Rosenberg, C.L., Handy, M.R., 2005. Experimental deformation of partially melted granite revisited: Implications for the continental crust. J. Metamorph. Geol. 23, 19–28. https://doi.org/10.1111/J.1525-1314.2005.00555.X.
Shao, Y., Piazolo, S., Liu, Y., Lee, A.L., Jin, W., Li, W., Liang, C., Wen, Q., 2021. Deformation behavior and inferred seismic properties of tonalitic migmatites at the time of pre-melting, partial melting, and post-solidification. Geochem. Geophys. Geosyst. 22, e2020GC009202 https://doi.org/10.1029/2020GC009202.
Stuart, C.A., Piazolo, S., Daczko, N.R., 2016. Mass transfer in the lower crust: Evidence for incipient melt assisted flow along grain boundaries in the deep arc granulites of Fiordland, New Zealand. Geochem. Geophys. Geosyst. 17, 3733–3753. https://doi.org/10.1002/2015GC006236.
Stuart, C.A., Daczko, N.R., Piazolo, S., 2017. Local partial melting of the lower crust triggered by hydration through melt–rock interaction: an example from Fiordland, New Zealand. J. Metamorph. Geol. 35, 213–230. https://doi.org/10.1111/jmg.12229.
Stuart, C.A., Piazolo, S., Daczko, N.R., 2018. The recognition of former melt flux through high-strain zones. J. Metamorph. Geol. 36, 1049–1069. https://doi.org/10.1111/JMG.12427.
Varga, J., Raimondo, T., Daczko, N.R., Adam, J., 2020. Experimental alteration of monazite in granitic melt: Variable U–Th–Pb and REE mobility during melt-mediated coupled dissolution-precipitation. Chem. Geol. 544, 119602.
Vernon, R.H., 2011. Microstructures of melt-bearing regional metamorphic rocks. Geol. Soc. Am. Memoirs 207, 1–11.
Walte, N.P., Bons, P.D., Passchier, C.W., 2005. Deformation of melt-bearing systems—insight from in situ grain-scale analogue experiments. J. Struct. Geol. 27, 1666–1679. https://doi.org/10.1016/J.JSG.2005.05.006.
Weinberg, R.F., Veveakis, E., Regenauer-Lieb, K., 2015. Compaction-driven melt segregation in migmatites. Geology 43, 471–474. https://doi.org/10.1130/G36562.1.
Wheeler, J., Mariani, E., Piazolo, S., Prior, D.J., Trimby, P., Drury, M.R., 2009. The weighted Burgers vector: a new quantity for constraining dislocation densities and types using electron backscatter diffraction on 2D sections through crystalline materials. J. Microsc. 233, 482–494. https://doi.org/10.1111/j.1365-2818.2009.03136.x.
Wheeler, J., Piazolo, S., Prior, D.J., Trimby, P.W., Tielke, J.A., 2024. Using crystal-lattice distortion data for geological investigations: the weighted Burgers vector method. J. Struct. Geol. 179, 105040.
Whitney, D.L., Samuelson, W.J., 2019. Crystallization sequences of coexisting andalusite, kyanite, and sillimanite, and a report on a new locality: Lesjaverk, Norway. Eur. J. Mineral. 31, 731–737. https://doi.org/10.1127/EJM/2019/0031-2873.
Yang, P., Rivers, T., 2001. Chromium and manganese zoning in pelitic garnet and kyanite: Spiral, overprint, and oscillatory (?) zoning patterns and the role of growth rate. J. Metamorph. Geol. 19, 455–474. https://doi.org/10.1046/J.0263-4929.2001.00323.X.
Yardley, B.W.D., Rochelle, C.A., Barnicoat, A.C., Lloyd, G.E., 1991. Oscillatory zoning in metamorphic minerals: an indicator of infiltration metasomatism. Mineral. Mag. 55, 357–365. https://doi.org/10.1180/MINMAG.1991.055.380.06.
Zibra, I., Kruhl, J.H., Montanini, A., Tribuzio, R., 2012. Shearing of magma along a high-grade shear zone: Evolution of microstructures during the transition from magmatic to solid-state flow. J. Struct. Geol. 37, 150–160. https://doi.org/10.1016/J.JSG.2012.01.011.